

**SHEAR RHEOLOGY OF CONCENTRATED EMULSIONS AT FINITE
INERTIA: A NUMERICAL STUDY**

by

Priyesh Srivastava

A thesis submitted to the Faculty of the University of Delaware in partial fulfillment of the requirements for the degree of Master of Science in Mechanical Engineering

Summer 2013

© 2013 Priyesh Srivastava
All Rights Reserved

**SHEAR RHEOLOGY OF CONCENTRATED EMULSIONS AT FINITE
INERTIA: A NUMERICAL STUDY**

by

Priyesh Srivastava

Approved: _____
Kausik Sarkar, Ph.D.
Professor in charge of thesis on behalf of the Advisory Committee

Approved: _____
Suresh Advani, Ph.D.
Chair of the Department of Mechanical Engineering

Approved: _____
Babatunde A. Ogunnaike, Ph.D.
Interim Dean of the College of Engineering

Approved: _____
James G. Richards, Ph.D.
Vice Provost for Graduate and Professional Education

ACKNOWLEDGMENTS

I would like to express my gratitude towards my advisor Dr. Kausik Sarkar for his guidance and support during my entire graduate study. My ability to study a research problem independently has significantly improved while working under him. It is easy for a student to get bogged down by the small details of research and his patient advice helped me to stay on track.

I am extremely thankful to Prof. Ajay Prasad and Prof. L.P. Wang for agreeing to be a part of my thesis committee. Prof. Prasad with whom I took a course on Fuel Cells provided me valuable advice from time to time and I am thankful to him for his support and encouragement. Prof. Wang with whom I took a course on Mesoscopic CFD played an instrumental role in developing my aptitude for numerical methods. The enthusiasm he displayed while teaching this course had a profound impact on me. Finally I would also like to acknowledge the stimulating intellectual experiences provided by Prof. Errol Lloyd, Prof. Valery Roy and Prof. Michael Greenberg during my MS coursework.

I am very thankful to the members of my research group: Shirshendu Paul, Dr. Rajesh Singh, Krishna Nandan, Dr. Swarnajay Mukherjee and Dr. Amit Katiyar, who have been extremely helpful during my graduate study. A special mention of my friends Jayanta Phadikar and Parag Nittur for all their help during my early days in Delaware. I would also like to thank my family members for their help and support.

I acknowledge the financial support from the National Science Foundation and the Mechanical Engineering department.

TABLE OF CONTENTS

LIST OF TABLES	vii
LIST OF FIGURES	viii
ABSTRACT	xi
 Chapter	
1 INTRODUCTION	1
1.1 Emulsion Rheology	2
1.2 Motivation and Scope	7
2 MATHEMATICAL MODELLING OF THE SYSTEM	9
2.1 Governing Equations for the One Liquid Formulation	9
2.2 Non-Dimensional Parameters	10
3 COMPUTATIONAL METHOD: FRONT TRACKING	13
3.1 Front Tracking Method	14
3.2 Surface Tension Calculation	14
3.3 Moving Mesh to Fixed Mesh Interpolation	16
3.4 Density and Viscosity Field	17
3.5 Navier Stokes Equation Solver	17
3.6 Advection of the Fronts	18
3.7 Parallelization	19
4 RHEOLOGY	21
4.1 Batchelor Stress Formulation	21
4.2 Interfacial Stress	23
4.3 Reynolds Stress	24
4.4 Effective Properties	25
4.4.1 Effective viscosity	25

4.4.2	Normal stress differences	25
4.5	Previous Rheological Results	26
4.5.1	Newtonian liquids	26
4.5.2	Emulsion: Stokes flow	27
4.5.3	Rigid particle suspension	27
4.5.4	Dilute emulsion: Finite inertia	28
5	STEADY SHEAR RHEOLOGICAL RESULTS	29
5.1	Validation	30
5.2	Concentrated Emulsion	31
5.3	Grid Resolution	34
5.4	Drop Number Dependence	37
5.5	Initial Position	39
5.6	Comparisons with Numerical Results	40
5.7	Dependence of the Interfacial Stresses on Reynolds Number	43
5.8	Capillary Number Variation	54
5.9	Reynolds Stresses	56
5.10	Excess Stresses	62
5.11	Relaxation Times	67
6	ALTERNATE DIRECTION IMPLICIT METHOD	69
6.1	Formulation	69
6.2	Procedure	70
6.3	Validation	71
6.4	Computational Costs	73
6.5	Conclusion	73
7	SUMMARY AND FUTURE WORK	74
7.1	Summary	74
7.2	Future Work	75
7.2.1	Shear-induced self-diffusion	76
7.2.2	Rheology in poiseulle flow	76
	REFERENCES	77

Appendix

A REPRINT PERMISSION LETTERS 82
A.1 Reprint Permission of Figure 1.3 (Chapter 1) 82

LIST OF TABLES

5.1	Table showing the grid resolution test for $\phi = 20\%$, $Re=1.0$ and $Ca=0.05$	36
5.2	Table showing the grid resolution test for $\phi = 20\%$, $Re=1.0$ and $Ca=0.20$ (average values only)	36
5.3	Table showing the grid resolution study for $\phi = 0.05\%$, $Re=1.0$ and $Ca=0.05$	36
5.4	Table showing the drop's number study for $\phi = 20\%$, $Re=1.0$ and $Ca=0.05$	38
5.5	Table showing relative domain size influence for $\phi = 20\%$, $Re=1.0$ and $Ca=0.05$	38
5.6	Table showing the drop's number study for $\phi = 20\%$, $Re=1.0$ and $Ca=0.20$	39
5.7	Table showing the drop's number study for $\phi = 20\%$, $Re=5.0$ and $Ca=0.05$ (average values only)	39
5.8	Table showing the drop's number study for $\phi = 0.05\%$, $Re=1.0$ and $Ca=0.05$ (average values only)	39
5.9	Table showing relaxation time for a single drop problem, $Re=0.05$ fixed	67
5.10	Table showing relaxation time for $\phi = 20\%$, $Re=0.10$ fixed	68
6.1	Table showing the computational cost of the ADI method	73

LIST OF FIGURES

1.1	Common examples of emulsions	1
1.2	A representative element of emulsion under shearing conditions . .	3
1.3	Microstructure of a sheared emulsion	5
2.1	Two-phase system.	11
3.1	Problem set-up	13
3.2	Fixed mesh	14
3.3	Moving mesh	14
3.4	Calculation of the surface tension force	15
4.1	Interfacial tensor calculation	24
4.2	Rod climbing effect	26
4.3	Shear rheology for a Newtonian liquid	27
4.4	Shear rheology for an emulsion under Stokes flow	28
5.1	Schematic diagram showing the computational domain	29
5.2	Comparison of the simulation and C-S model	31
5.3	Time variation of N_1^{int}	33
5.4	Time variation of N_2^{int}	33
5.5	Time variation of Σ_{xy}^{int}	33
5.6	Grid resolution test for N_1	34

5.7	Grid resolution test for Σ_{xy}	35
5.8	Influence of the initial drops' positions	40
5.9	Comparisons of interfacial stress with the simulations of Lowenberg and Hinch ($\phi=20\%$)	42
5.10	Comparisons of interfacial stress with the simulations of Zinchenko and Davis ($\phi=30\%$)	42
5.11	Variation of N_1^{int} with Re and ϕ at Ca=0.05	43
5.12	Variation of N_2^{int} with Re and ϕ at Ca=0.05	44
5.13	Variation of Σ_{xy}^{int} with Re and ϕ at Ca=0.05	45
5.14	Connection between orientation and normal stress differences	46
5.15	Variation of the average orientation with Re and ϕ (Ca=0.05)	48
5.16	Taylor deformation parameter	49
5.17	Variation of the average deformation with Re and ϕ (Ca=0.05)	50
5.18	N_1^{int} variation with Re over a range of Ca. ($\phi= 20\%$ fixed)	52
5.19	N_2^{int} variation with Re over a range of Ca. ($\phi= 20\%$ fixed)	53
5.20	Σ_{xy}^{int} variation with Re over a range of Ca. ($\phi= 20\%$ fixed)	53
5.21	Interfacial stresses variation with Ca ($\phi=20\%$, Re=1.0)	55
5.22	Average deformations and orientations variations with Ca ($\phi=20\%$, Re=1.0)	55
5.23	Velocity profile $\phi=0.20$, Re10, Ca0.05	57
5.24	Average velocity of drops' centers $\phi=0.20$, Re1, Ca0.05	57
5.25	Reynolds stresses dependence on ϕ (Ca=0.05 and Re=1.0)	58
5.26	Reynolds stresses dependence on Re ($\phi=0.20\%$ and Ca=0.02)	58

5.27	Reynolds stresses dependence on Re ($\phi=0.20\%$ and $Ca=0.075$) . . .	59
5.28	Perturbation stresses dependence on Re ($\phi=0.20\%$ and $Ca=0.05$) .	60
5.29	Time evolution of R_{xx} for different Re ($\phi=0.20\%$ and $Ca=0.05$) . .	60
5.30	Time evolution of R_{yy} for different Re ($\phi=0.20\%$ and $Ca=0.05$) . .	61
5.31	Reynolds stresses dependence on Ca ($\phi=0.20\%$ and $Re=1.0$)	62
5.32	N_1^{excess} variation with Re ($Ca=0.05$ fixed)	63
5.33	N_2^{excess} variation with Re ($Ca=0.05$ fixed)	64
5.34	Σ_{xy}^{excess} variation with Re ($Ca=0.05$ fixed)	64
5.35	Dependence of the stresses on volume fraction ($Re=1.0$ and $Ca=0.05$)	66
5.36	Dependence of the viscosity on volume fraction ($Re=1.0$ and $Ca=0.05$)	66
6.1	Validation of the ADI scheme with the first case	72
6.2	Validation of the ADI scheme with the second case	72

ABSTRACT

The dynamics and rheology of an emulsion of viscous drops in shear flow is investigated computationally. The simulations are performed using a three-dimensional front tracking method. An emulsion gives rise to an effective non-Newtonian rheology with finite normal stress differences and shear-dependent viscosity.

Previous estimates about the bulk properties of emulsions were limited to Stokes conditions under which a positive first normal stress difference and a negative second normal stress difference are predicted. However, the introduction of finite inertia significantly modifies the behaviour of emulsions. The normal stress differences change sign and the emulsion shows a shear-thickening behaviour with inertia. Computed rheological properties (effective shear viscosity and first and second normal stress differences) in conditions close to Stokes limit match well with the existing theoretical and simulated results. The first component of the rheology arising from the interfacial stresses at the drop surface is investigated as functions of particle Reynolds number, capillary number and volume fraction. The sign change is caused by the increase in drop inclination in presence of inertia, which in turn directly affects interfacial stresses due to drops. Increasing volume fraction or capillary numbers increases the critical Reynolds numbers for sign reversals due to increasing alignment of the drops with the flow directions. The Reynolds stresses which form the second component of the stress formulation are also considered in detail. The primary components of the Reynolds stress showed a simple scaling with Reynolds number for moderate values of inertia. They showed a non-linear increase at larger values of Reynolds number. A comparison of the estimated effective viscosity with an established empirical relation is also presented.

Presence of finite surface tension results in a characteristic stress relaxation time scale for emulsions. This is investigated for both dilute and concentrated systems and the results are verified against the standard theoretical expressions. Finally, to enhance the capabilities of the current computational method to handle extremely low Reynolds number flows, a parallel version of the Alternate Direction Implicit method is implemented.

Chapter 1

INTRODUCTION

Emulsions which are a mixture of two or more immiscible liquids are ubiquitous in our day to day life. They find numerous applications in different mechanical and chemical engineering industries such as in the oil extraction process, food processing, pharmaceutical manufacturing, etc. The properties of emulsions are determined by their constituting phases as well as their internal arrangement. The small scale arrangement of the constituting phases is termed as the microstructure [1]. Emulsions of desirable mechanical properties can be obtained by manipulating their small scale morphology [2]. Consequently it is of significant importance to establish the close connection between the bulk properties of emulsions and their microstructure.



(a) Milk (commons.wikimedia.org)

(b) Mayonnaise (commons.wikimedia.org)

Figure 1.1: Common examples of emulsions

The following section outlines some of the research attempts that have been made to predict the effective properties of emulsions by understanding the above mentioned link. The subsequent section provides a motivation and the main objectives of the present work.

1.1 Emulsion Rheology

It is of great practical importance to understand the behaviour a complex liquid like emulsion under different geometries and flow conditions. The solution to the velocity and pressure fields (which essentially describe the behaviour of the liquid) under a particular fluid flow would require a general stress-strain rate relationship. This is well established for a simple Newtonian liquid like water phenomenologically, where a single viscosity coefficient is sufficient to describe the relationship. A similar constitutive equation for emulsions is very difficult to determine phenomenologically. So a possible approach is to derive them from first principles by resolving the small scales as well. Derivation of the constitutive equations from first principles under general flow conditions can be a very complicated problem. However valuable insights into the behaviour of emulsions can be obtained by studying the constitutive relations under simple flow conditions such as steady shear flow, extensional flow and oscillatory flow. Steady shearing type of flows impose a constant shearing condition at the macroscale and its impact on the microscale is calculated. Extensional flow imposes a vorticity free condition and oscillatory flow imposes a time varying condition. Among these flow fields, steady shear flow conditions can be achieved in experiments easily (e.g. cone and plate rheometer). Consequently a significant amount of research efforts have been focussed on the development of constitutive equations (by resolving the smaller scales) under steady shearing conditions.

The earliest work relating the effective properties of emulsion to its internal micro-structure dates back to the seminal work of Taylor [3] in which he derived the effective viscosity of a dilute emulsion under small deformation conditions. This was an extension for the Einstein's viscosity [4] expression for a rigid particle suspension.

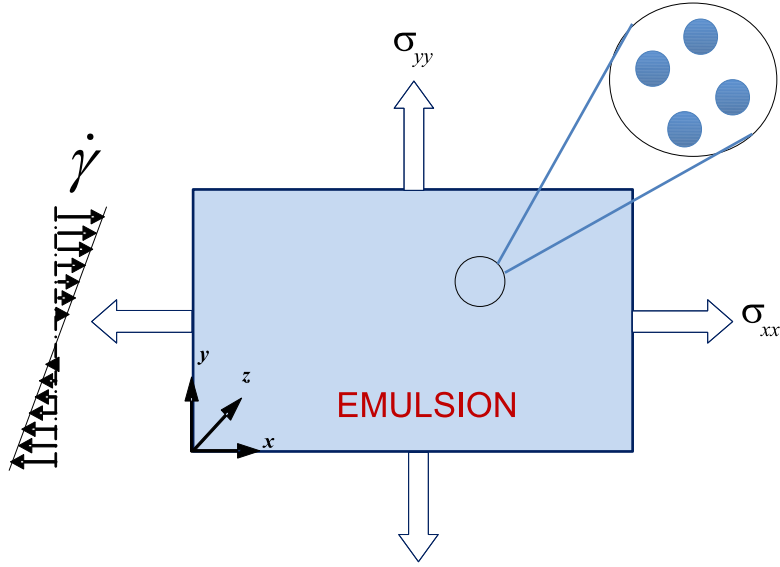


Figure 1.2: A representative element of emulsion under shearing conditions

Using perturbative methods and assuming a Stokes flow condition Taylor predicted the following expression for effective viscosity:

$$\mu^{eff} = \mu \left[1 + 2.5\phi \left(\frac{\lambda + \frac{2}{5}}{\lambda + 1} \right) \right]$$

This was a zeroth order result and assumed spherical shapes of the drops. Consequently it did not predict the presence of normal stress differences. Oldroyd [5] considered the elastic properties of the emulsion and assumed a linear stress-strain relation which involved their time derivatives as well. Using perturbation techniques he obtained the Taylor's viscosity expression (this was also a zeroth order solution) and also found the relaxation and retardation times. These time scales are another characteristic behaviour of non-Newtonian fluids. Schowalter et al. [6] obtained expressions for the normal stress differences by solving the first order perturbative solutions. They took into consideration the deviations in the spherical shape of the drop. Using perturbation

techniques Frankel et al. [7] developed the general expressions of the stress tensor of an emulsion in a time dependent shearing flow. From the general expressions, they matched with the existing published results as special cases. Choi and Schowalter [8] extended the results for a semi dilute system. They used a cell model approach to account for the inter-drop interactions and gave an order ϕ^2 expression for the shear stress and the normal stress differences.

The approach adopted by the previous papers was essentially a perturbative one and the results were mostly valid under their assumed asymptotic conditions. Certain semi-phenomenological approach which involve some modelling at the small scales have achieved success in the prediction of the behaviour of emulsions under more general conditions. These methods are based on the modelling of the time evolution of tensorial quantities which capture the geometry of the dispersed drops. Doi and Ohta [9] developed such a model for bi-continuous blend with a 50% volume fraction. They divided the time dependence of the geometric tensors as additive contributions from drop relaxation (surface tension) and drop deformation (external flow deformation). Since the formulation was for bi-continuous blend, the model lacked an intrinsic length/time scale. Using their model they obtained a linear relationship between stresses and velocity gradient. Following this work, various modifications were made to the Doi-Ohta model and a review of those is avoided here. Maffettone and Minale [10] developed a similar phenomenological model assuming an ellipsoidal shape for the drop. They compared the prediction of their model with experiments for the drop deformation and orientation in shear flow for a range of Capillary numbers. Almusallam and coworkers [11] proposed a phenomenological model where the volume of the drops were conserved and so their model had an intrinsic length/time scale. They obtained good agreement of the drop shape evolution with experiments.

Numerical simulations offer a good alternative approach where most of the assumptions of the theoretical models can be relaxed. Computational techniques like Stokesian dynamics [13] have been successful in the prediction of rheology of rigid particle suspensions and have provided a deep insight into the internal structure of



Figure 1.3: Microstructure of a sheared emulsion (Reprinted with permission from Iza & Bousmina (2000) [12]. © 2000, The Society of Rheology)

suspensions. Stokesian dynamics has been employed for understanding the behaviour and dynamics of Brownian as well as non-colloidal suspensions of hard spheres under Stokes flow condition. They predict a range of non-Newtonian behaviour which arise due to the break down of the reversibility of Stokes flow. A suspension of hard spheres under low Peclet condition (which is a measure of the relative strengths of hydrodynamics and Brownian forces) exhibit shear thinning and a positive first normal stress difference and a negative second normal stress difference. Increasing Peclet number modifies the behaviour of the system. As the relative strength of the hydrodynamic forces increase the suspension exhibits shear thickening and the first normal stress difference becomes negative. The shear thickening occurs because of the formation of the hydrodynamic clusters [14]. There also have been some recent experimental confirmation of the existence of finite normal stress differences in the case of non-colloidal suspensions [15].

In case of deformable particle suspensions, numerical simulations have been fewer as they are computationally more intensive. Secondly, numerical simulations

generally do not take into account the complicated phenomena like the drops coalescence and breakup. Therefore it gets difficult to match up these results with realistic experiments. Zhou and Pozrikidis [16] studied the dynamics of two-dimensional periodic and random suspensions in closed channels using numerical simulations. Lowenber and Hinch [2] did boundary integral simulations of concentrated emulsions. They provided deep insight into the connection between the small scale morphology and the bulk properties. They predicted a shear thinning behaviour and a positive first normal stress difference and a negative second normal stress difference. In case of the drops (i.e. deformable particles) the deformation in the shape produces anisotropy in the flow field and the non-Newtonian behaviour can be explained by considering simple parameters like orientations and deformations. Zinchenko and Davis [17] did boundary integral simulations of highly concentrated emulsions and discussed in detail about selecting the correct parameters for accurately predicting the rheology. They computed the dependence of the normal stress differences and shear stress on capillary number for very high volume fractions and noticed that most of the shear thinning at very high concentrations occur at small deformation conditions.

Investigation of the dynamics and rheology of emulsions and suspensions in presence of finite inertia has been quite limited. Lin and Scholwater [18] accounted for the effect of finite fluid inertia on the rheology of rigid particle suspensions (dilute system). They assumed a condition of zero forces and torques on the particles and using asymptotic techniques they found that the effect of inertia was to produce a negative first normal stress difference. Patankar et al. [19], performed two dimensional simulations for a similar system where they included finite forces on the particle. They also predicted a negative first normal stress difference and a shear thickening behaviour. Using a volume of fluid method, Renardy et al. [20] studied the effect of inertia on the geometry and break of a single drop under shear flow condition. Li and Sarkar [21] investigated the influence of increasing inertia on the rheology of a dilute emulsion (i.e. a single drop) using front tracking simulations. They predicted the reversal of the signs of normal stress differences with increasing Reynolds number. A similar study

was also pursued by Raja et al. [22] analytically and they found qualitatively similar results. Singh and Sarkar [23] found out that the normal stress differences change their signs with Reynolds number only for a range of capillary numbers. These studies have however been limited to a dilute system i.e. a single drop problem.

Numerical simulations of the dynamics of emulsions is essentially a two phase (or multiphase if generalized more) flow problem. Currently a number of sophisticated techniques are available for the simulations of such a problem. Some of the popular methods among them are the volume of fluid method [24], level set [25], a coupled level set and volume of fluid method [26] and front tracking method [27]. Front tracking though computationally more expensive than the other methods provides a very accurate tracking of the drop's motion and prevents the artificial diffusion of the interfaces between the separate phases. Consequently it has been extensively used for studying multiphase flow problems [28–37]. Recently Lattice Boltzmann method [38] has also made significant advances on the simulation of deformable particle suspensions [39].

1.2 Motivation and Scope

The objective of the present work is to study the behaviour and effective properties of a concentrated emulsion in steady shear. The focus of the research is to understand the effects of inertia and concentration on the effective rheology of emulsions. It is a simple system, consisting of mono-dispersed Newtonian drops in a Newtonian matrix. The bulk properties of the emulsion are estimated by volume averaging the microscopic quantities as proposed by the Batchelor stress formulation [40]. The formulation assumes that the scale of the macroscopic flow is larger than the size of the droplets. This means that we can find an averaging volume element smaller than the macroscopic flow scales and much larger than the droplet size. The coalescence and breakup have not been considered. Nevertheless, the simple system provides valuable insights about emulsions and exhibits a number of non-Newtonian properties such as shear thinning and presence of non-zero normal stress differences. It captures the effects of increasing concentration and demonstrates that presence of small amount of

inertia can qualitatively change the rheological behaviours such as a change of the signs of normal stress differences.

Chapters 2 and 3 provide the details of the mathematical modelling of the problem and the numerical method used for its solution. Chapter 4 presents the background required for understanding the idea of rheology and finally chapter 5 presents the results of this study. Chapter 6 discusses about the implementation of a parallel version of the Alternate Direction Implicit method which will enhance the capability of the code to deal with extremely low Reynolds number flows. Some of the possible future works are provided in chapter 7.

Chapter 2

MATHEMATICAL MODELLING OF THE SYSTEM

The emulsion is modelled as a mixture of spherical droplets dispersed in a matrix fluid. The drops are mono-dispersed i.e. every drop has identical shape, size and property. The matrix liquid and the droplets are considered as Newtonian fluid. This essentially is a two phase system (see fig 2.1). This problem can be approached by solving separate sets of Navier Stokes equations for the matrix fluid and the droplets and connecting them via appropriate boundary conditions at the drops' interface. An alternate to this approach is to pose this problem as a single fluid formulation. This can be done by including the surface tension force as a body force term in the momentum equation. This body force term involves a dirac delta function which ensures that the boundary conditions are felt only at the interface of the drops.

2.1 Governing Equations for the One Liquid Formulation

The derivation of the one liquid formulation is avoided here. The key idea behind this approach is the use of dirac delta functions to convert surface integrals to volume integrals. The formulation consists of the following set of equations:

Continuity equation

$$\nabla \cdot \mathbf{u} = 0 \quad (2.1)$$

Momentum equation

$$\frac{\partial(\rho \mathbf{u})}{\partial t} + \nabla \cdot (\rho \mathbf{u} \mathbf{u}) = -\nabla p + \nabla \cdot [\mu \{ \nabla \mathbf{u} + (\nabla \mathbf{u})^T \}] - \int_{\partial B} \kappa \mathbf{n} \Gamma \delta(\mathbf{x} - \mathbf{x}') dS(\mathbf{x}') \quad (2.2)$$

State equation

$$\frac{D\rho}{Dt} = 0 \tag{2.3}$$

$$\frac{D\mu}{Dt} = 0 \tag{2.4}$$

For the above set of equations \mathbf{u} is the fluid velocity, ρ and μ are the density and viscosity respectively which take appropriate values for the matrix liquid and the droplets, Γ is surface tension and κ is the local curvature of the droplets. The first equation specifies that both the liquids are incompressible. The momentum equation has a surface tension force as an area integral (integrated over the surface of drops). It is this term which captures the two fluid system in a single equation. The last two equations specify that the density and viscosity for each liquid is constant.

2.2 Non-Dimensional Parameters

The dynamics of this two phase system is governed by a number of non-dimensional parameters. The analysis that will be presented in the later sections is reported in terms of these parameters. The non-dimensional parameters are:

Reynolds number: The velocity scale is formed using the imposed shear rate and the drop's radius. The length scale is taken as the drop's radius itself.

$$\text{Reynolds number (Re)} = \frac{\rho_0 \dot{\gamma} a^2}{\mu_0}$$

Capillary number: The capillary number indicates the strength of the deforming viscous stresses acting on the drops relative to the restoring surface tension force.

$$\text{Capillary number (Ca)} = \frac{\mu_0 \dot{\gamma} a}{\Gamma}$$

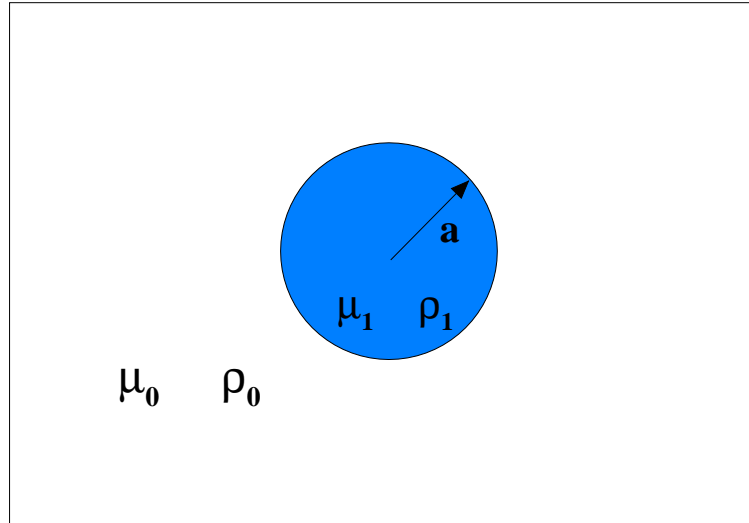


Figure 2.1: Two-phase system.

Volume fraction: This is the fraction of the volume constituted by the dispersed droplets.

$$\text{Volume fraction}(\phi) = \frac{4\pi a^3 N}{3V} \quad (2.5)$$

Density ratio: This is the ratio of the drop and matrix liquid density. This parameter will be fixed at unity for the entire study.

$$\text{Density ratio}(\lambda_p) = \rho_1/\rho_0$$

Viscosity ratio: It is the ratio of the drop and matrix liquid viscosity. This parameter is also fixed at unity for the entire study.

$$\text{Viscosity ratio}(\lambda) = \mu_1/\mu_0$$

Chapter 3

COMPUTATIONAL METHOD: FRONT TRACKING

As mentioned before the emulsion is modelled by dispersing spherical drops in a matrix liquid and the objective is to study the bulk properties of the system under shearing condition. This is achieved via numerical simulations and the problem set up is shown in the figure below. Figure 3.1 below shows the three dimensional domain in which spherical drops are suspended in an ambient fluid. The domain is periodic in x-direction and z-direction. It is subjected to wall boundary conditions along the y-direction. The top and bottom walls move with a constant speed U in opposite directions. This imposes a shearing condition, the flow condition under which we are interested in investigating the effective properties of the emulsion. The system is mathematically modelled using the single fluid formulation outlined in the previous chapter.

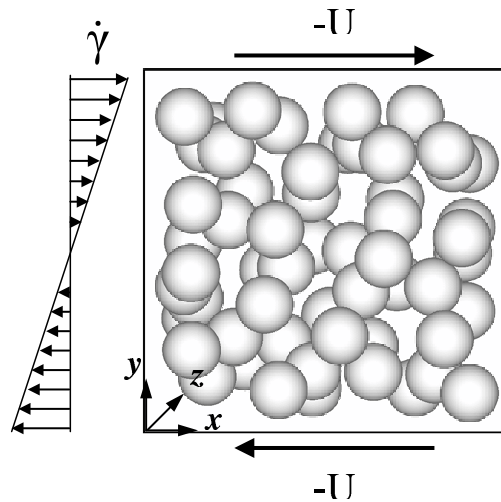


Figure 3.1: Problem set-up

Commonly used methods for solving the single fluid formulation such as the volume of fluid method involves an extra scalar for distinguishing the two liquids. This extra scalar satisfies an advection equation. Using this approach the entire set of equations is solved on a single fixed mesh. The computational method used presently is a front tracking method and it does not use an extra scalar for distinguishing the two liquids. It involves a second moving mesh for explicitly tracking the motion of the drops. The front tracking method is outlined in detail in the following sections.

3.1 Front Tracking Method

This computational method uses two separate mesh for simulating the flow. The first is a fixed cartesian mesh on which the set of Navier stokes equations are solved. The second mesh is a moving mesh that explicitly tracks the motion of the drops. This is a surface mesh and is composed of triangular elements. Figures 3.2 and 3.3 below show the two meshes.

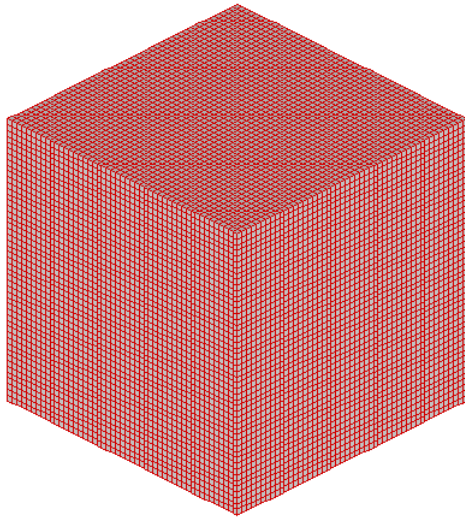


Figure 3.2: Fixed mesh

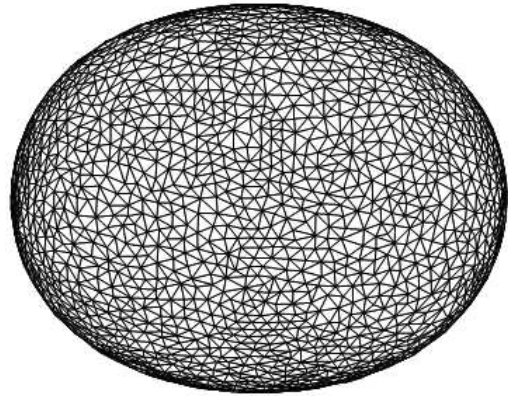


Figure 3.3: Moving mesh

3.2 Surface Tension Calculation

Along with tracking the motion of the drops, the surface mesh is also used for calculating the surface tension force. This force is calculated as a surface force term

on the moving mesh. Figure 3.4 shows a typical triangular element along with its adjoining neighbours. The surface tension force on an element \mathbf{a} is given by the surface integral:

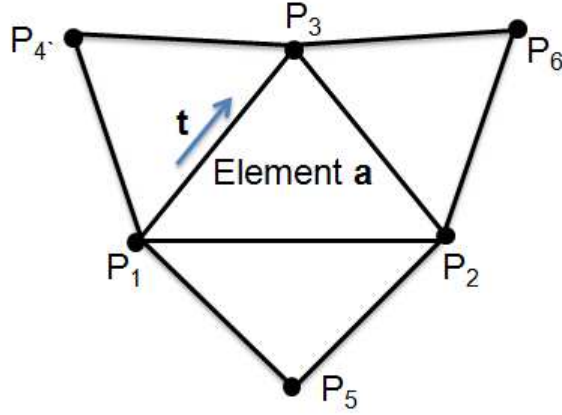


Figure 3.4: Calculation of the surface tension force

$$\partial F_a = \Gamma \int_{\partial A} \kappa \mathbf{n} dA = \Gamma \oint_S (\mathbf{t} \times \mathbf{n}) dS$$

Here Γ is the surface tension coefficient, κ is the curvature, \mathbf{t} is the tangential vector (shown in the figure) and \mathbf{n} is the normal to the surface. The surface integral is a well known result and it has been converted into a line integral using Stokes theorem. The surface tension force is calculated using the line integral. The tangential vector \mathbf{t} is calculated easily by finding the unit vectors aligned along the edges of the element. The calculation of the normal vector involves a quadratic surface fitting. A quadratic surface of the form shown below is fitted through the nodal points of the element \mathbf{a} and the nodal point of the three adjoining elements.

Quadratic surface

$$z = ax + by + cxy + dx^2 + ey^2$$

Once the quadratic fitting is completed the gradient of the surface gives the normal vector which is then plugged in the previous expression for the surface tension force. This completes the evaluation of the surface tension force on every such element \mathbf{a} .

3.3 Moving Mesh to Fixed Mesh Interpolation

The surface tension force calculated on the moving mesh is a surface force and the one fluid formulation requires this force as a body force term on the fixed mesh. This necessitates the interpolation of the surface tension force from the moving mesh to the fixed mesh. The key idea behind this is that the total strength of the interpolated quantity should remain conserved, which in turn provides the relation for the interpolated body force term on the fixed mesh.

$$\int_S \phi_f(\mathbf{x}') dS' = \int_V \phi_g(\mathbf{x}) dV \implies \phi_g = \int_S \phi_f(\mathbf{x}') \delta(\mathbf{x} - \mathbf{x}') dS'$$

Here ϕ_f is the surface force calculated on the moving mesh and ϕ_g is the interpolated body force term on the fixed mesh.

The Dirac delta function $\delta(\mathbf{x} - \mathbf{x}')$ occurring in the previous relation is approximated by a function $D(\mathbf{x} - \mathbf{x}')$ which has a finite support i.e. having a finite width. This is done by using the Peskin Cosine [41] function which has a width of four grid spacing in each direction.

$$\delta(\mathbf{x} - \mathbf{x}') \approx D(\mathbf{x} - \mathbf{x}') = \prod_{i=1}^3 D^i(\mathbf{x} - \mathbf{x}')$$

$$D^i(\mathbf{x}_i - \mathbf{x}'_i) = \begin{cases} \frac{1}{4h_i} (1 + \cos \frac{\pi(\mathbf{x}_i - \mathbf{x}'_i)}{2h_i}) & |(\mathbf{x}_i - \mathbf{x}'_i)| < 2h \\ 0 & |(\mathbf{x}_i - \mathbf{x}'_i)| > 2h \end{cases}$$

3.4 Density and Viscosity Field

The densities and the viscosities of the matrix liquid and the drops can be different in general. So from a given location of the fronts, these scalar fields need to be created. The scalar fields will be required in the solution of Navier-Stokes equations. The scalar fields (of density and viscosity) are generated by determining their gradients by the following relation:

$$\nabla\phi(\mathbf{x}) = \int_S \Delta\phi\delta(\mathbf{x} - \mathbf{x}')\mathbf{n}dS'$$

Here ϕ can represent either density or viscosity. This equation can be integrated directly to obtain the appropriate scalar field. In the present code, divergence of the above equation is calculated, which results in a Poisson's equation. The resulting Poisson's equation is solved with a multigrid subroutine.

3.5 Navier Stokes Equation Solver

Once the density and viscosity field have been generated from the location of the fronts and the interpolated surface tension force has been estimated, all the components necessary for setting up the Navier Stokes equations are present. The set of Navier Stokes equations are solved explicitly on the fixed mesh using a projection method. In the first step of the projection method an intermediate velocity field is generated using the values of the previous time step.

$$\frac{\rho^{n+1}\mathbf{u}^* - \rho\mathbf{u}^n}{\delta t} = -\nabla \cdot (\rho\mathbf{u}\mathbf{u})^n + \nabla \cdot \tau^n + \mathbf{f}^n$$

Here the spatial derivatives are discretised using a second order central differencing scheme. \mathbf{f}^n is the interpolated surface tension force. The intermediate velocity field is used to create the pressure Poisson's equation which guarantees that the continuity

equation is satisfied.

$$\nabla \cdot \left(\frac{1}{\rho^{n+1}} \nabla p^{n+1} \right) = \frac{1}{\delta t} \nabla \cdot \mathbf{u}^*$$

The newly constructed field is then used for projecting the intermediate velocity field onto a divergence free velocity field, which is the new velocity field.

$$\frac{\mathbf{u}^{n+1} - \mathbf{u}^*}{\delta t} = -\frac{1}{\rho^{n+1}} \nabla p^{n+1}$$

The Poisson's equation arising in the previous step is solved using a geometric multigrid solver. Since this is an explicit scheme it suffers from different stability criteria. The convective restriction i.e. $\delta t < \frac{2.0\mu}{\rho U_{max}^2}$ and the CFL criteria of $\delta t < \frac{\delta x}{U_{max}}$ do not affect the simulations as the Reynolds numbers for the simulations are quite low. The viscous stability criteria: $\delta t < \frac{0.125\rho\delta x^2}{\mu}$ dictates the time stepping limit. This can be alleviated to some extent by including some of the viscous terms implicitly and this approach is called the Alternate Direction Implicit (ADI) method. The development of the parallel subroutines for ADI was a separate part of the research and will be discussed in a later chapter. The results for the emulsion rheology do not include the ADI subroutines.

The solution of the set of Navier-Stokes equations gives the updated velocity field on the fixed mesh. The advection of the front requires this time an interpolation from the fixed mesh to moving mesh and this is discussed in the following section.

3.6 Advection of the Fronts

Once the updated velocity field have been calculated it has to be interpolated on the moving mesh to advect the fronts. This is achieved by the use of the following

relation:

$$\mathbf{u}(\mathbf{x}_f) = \int_V \mathbf{u}(\mathbf{x}) \delta(\mathbf{x} - \mathbf{x}_f) dV$$

$$\mathbf{x}_f^{n+1} = \mathbf{x}_f^n + \mathbf{u}(\mathbf{x}_f) \delta t$$

The delta function is again numerically approximated by using the Peskin Cosine function. The advection of fronts may lead to a decrease or increase in the size of the front elements. This may result in “ poor front quality ” and this is prevented in the code by employing an adaptive regridding. Certain threshold limits are placed below or above which the sizes of the elements cannot decrease or increase respectively. The details of this is avoided here and the reader is directed to the paper by Trygvasson et al. [27].

3.7 Parallelization

The front tracking code that is used for the simulations has been parallelized using MPI libraries. A domain decomposition methodology is used for the fixed mesh on which the set of Navier Stokes equations are solved. The entire domain is subdivided into a number of smaller sub-domains and a processor is attached to each subdomain. Since the Navier Stokes equations are solved explicitly the parallelization of the Navier Stokes solver on the fixed mesh is relatively easy.

The calculation of the front quantities such as the surface tension force uses a different methodology. It uses a Master-Slave approach where each front has associated with it a master processor. The master processor does all the calculation for its associated front and then it passes this information to the remaining slave processors associated with the front. The master processor is determined by finding out the sub-domain on the fixed mesh which has the maximum number of nodal points of a front. The processor associated with that sub-domain becomes the master processor of that front. The processors of the remaining sub-domains which share some of the nodal points of the given front become the slave processors. The master processor does all the calculation associated with the given front and then it passes this information to

the slave processors. The slave processor uses this information for the interpolation between the moving and fixed mesh. The reader is directed to the following reference [42] for the details of this procedure and the scalability of the code.

Chapter 4

RHEOLOGY

The previous chapters gave a brief description of our problem and the computational method used for simulating the fluid flow. The present chapter will discuss in detail about the physical quantities we are interested in calculating. The procedure used for estimating these quantities will also be discussed.

The main goal of a rheological study is to develop the constitutive equations of a complex liquid. This can be stated as the following question: We have a homogeneous fluid. We take a representative element of the fluid subjected to given strain rates. What are the stresses developed on the faces of this element? This question is well answered for a Newtonian liquid like water phenomenologically. Such a general stress-strain relationship for a complex liquid like emulsion is very hard to formulate. As it was mentioned in the preceding chapters, the constitutive equations are derived from the first principles under simple flow conditions and this gives us a valuable insight into the dynamics of such liquids. Steady shearing condition is one of the most commonly used type of flow for such a study and the present work is also completely focussed on shear rheology.

4.1 Batchelor Stress Formulation

Batchelor [40] gave a mathematical expression for determining the bulk properties of emulsions by establishing a connection between the macroscopic and microscopic quantities. Here macro-scale corresponds to the scale associated with the emulsion fluid flow and the micro-scale is that associated with the drop's motion. The key idea is to take a statistical approach in determining the bulk quantities. To determine the stress developed on the faces of a representative element of the emulsion subjected to

a given straining condition, an ensemble of such elements needs to be considered. The average of the stresses over all such ensembles gives the required stress which is termed as macroscopic stress. This is a macroscopic property in the sense that the scale over which they vary is governed by the macro-scales associated with the emulsion fluid flow. To evaluate the ensemble average, the property of ergodicity has to be invoked and the ensemble average is converted into an integral of the stresses over the volume of the representative element. This is expressed by the following relation:

$$\boldsymbol{\sigma}^{ave} = \int_V (\boldsymbol{\sigma} - \rho \mathbf{u}' \mathbf{u}') dV \quad (4.1)$$

Here V is the volume of the representative element being sampled. $\boldsymbol{\sigma}^{ave}$ is the macroscopic stresses developed and is called the average stress since it is estimated through an averaging process. The term $\boldsymbol{\sigma}$ inside the integration sign is the stress developed inside the emulsion element (i.e. the stress generated on the microscopic scale). The final term $\rho \mathbf{u}' \mathbf{u}'$ under the integration sign captures the additional momentum fluxes due to the disturbances generated by the presence of drops. This stress can be viewed as the Reynolds stress arising in turbulent flows and consequently is also called Reynolds stress. The details of this stress will be explained in the following sections. Equation 4.1 can also be written as a sum of the following terms:

$$\boldsymbol{\sigma}^{ave} = P^{ave} \mathbf{I} + \boldsymbol{\tau}^{ave} + \boldsymbol{\sigma}^{excess} \quad (4.2)$$

Here the left hand term is the average or macroscopic stress. The first two terms on the right hand side arise due to the macroscopic or bulk shearing. This can be obtained from the stress-strain relationship of the matrix liquid (which is Newtonian). The last term called the excess stress captures the effect of the presence of drops on the macroscopic stress and is a complicated quantity. This has to be calculated from numerical simulations.

Further mathematical manipulations show that the excess stresses can be broken

down into two terms:

$$\boldsymbol{\sigma}^{excess} = \frac{-\Gamma}{V} \sum \int_{A_d} (\mathbf{nn} - \frac{\mathbf{I}}{3}) dA + \frac{-1}{V} \int_V \rho \mathbf{u}' \mathbf{u}' dV \quad (4.3)$$

In the above expression the second term of the right hand side is the Reynolds stress which was explained before. It shows up as a part of the excess stress (and this should be as excess stress captures the effects of drops). The first term is called the interfacial stress. Both the above stresses are explained in detail in the section below.

4.2 Interfacial Stress

$$\boldsymbol{\sigma}^{int} = \frac{-\Gamma}{V} \sum \int_{A_d} (\mathbf{nn} - \frac{\mathbf{I}}{3}) dA \quad (4.4)$$

The interfacial stress defined above is one of the components of the stresses generated by the presence of drops. This is an interesting quantity as it is completely determined by the geometry of the drops. It does not involve any pressure or velocity terms. This quantity gives a measure of how much the drops are deformed and the direction along which they are oriented due to the imposed flow condition.

Figure 4.1 shows a snapshot of a drop inside the emulsion. The integral of the quantity $\Gamma(\mathbf{nn} - \frac{\mathbf{I}}{3})$ over the drop's surface is calculated. This requires the knowledge of the normal vectors over the drop's interface and this is already calculated as part of the front tracking method. The above quantity is computed for all the drops and the summation of them normalized with the volume of the element (being sampled) gives the interfacial stresses.

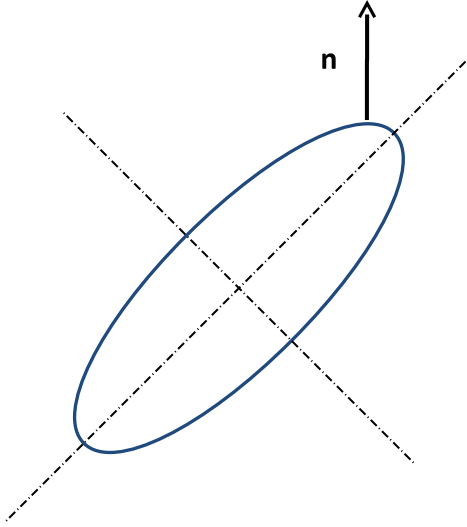


Figure 4.1: Interfacial tensor calculation

4.3 Reynolds Stress

$$\boldsymbol{\sigma}^{re} = \frac{-1}{V} \int_V \rho \mathbf{u}' \mathbf{u}' dV \quad (4.5)$$

$$\mathbf{u}' = \mathbf{U} - \bar{\mathbf{U}} \quad (4.6)$$

The Reynolds stress captures the disturbances in the velocity field produced by the presence of the drops. In the above equation \mathbf{U} represents the actual velocity field inside the element and $\bar{\mathbf{U}}$ is the bulk velocity. This quantity is similar to the Reynolds stress term arising in turbulent flows. The idea behind including this term is to include the additional momentum fluxes which were lost because of the averaging process.

4.4 Effective Properties

4.4.1 Effective viscosity

While studying the rheology of any complex liquid we are first of all interested in estimating its effective viscosity. The expression of the viscosity can be obtained from the equation 4.2 defined above for the calculation of the average stresses. The following expression gives this relation with the viscosity scaled with that of the matrix fluid.

$$\frac{\mu^{ave}}{\mu} = 1 + \frac{\sigma^{excess}}{\dot{\gamma}\mu} \quad (4.7)$$

4.4.2 Normal stress differences

Along with the effective viscosity we are interested in calculating the normal stress differences as defined below. Note that we are interested only in their differences and not the normal stresses themselves as both the liquids involved here are incompressible and the normal stresses can be determined only up-to a constant value for incompressible liquids.

$$N_1 = \sigma_{xx}^{ave} - \sigma_{yy}^{ave}$$
$$\frac{N_1}{\mu\dot{\gamma}} = \frac{\sigma_{xx}^{excess} - \sigma_{yy}^{excess}}{\mu\dot{\gamma}}$$

$$N_2 = \sigma_{yy}^{ave} - \sigma_{zz}^{ave}$$
$$\frac{N_2}{\mu\dot{\gamma}} = \frac{\sigma_{yy}^{excess} - \sigma_{zz}^{excess}}{\mu\dot{\gamma}}$$

From the above expressions it should be noted that the normal stress differences arise only due to the excess stresses (i.e. due to the presence of the drops). The bulk shearing terms do not produce any normal stress differences and this is because of the Newtonian nature of the matrix liquid.

The significance of the shear viscosity is easy to understand, it gives a measure of

the opposing shearing stresses that will be generated when an element of the emulsion is sheared. Presence of normal stress differences under shearing condition is sort of counter-intuitive. However in reality they affect the flow properties of the emulsion in a very perceptible way and they show up in a number of peculiar behaviours of complex liquids. A very good example of this would be the Weissenberg effect popularly referred to as “rod climbing effect”. Figure 4.2 below shows this. A Newtonian liquid when stirred moves away from the stirrer due to the centrifugal forces (left picture). However certain liquids move radially inward and actually climb up the rod (right picture). This is a manifestation of the normal stress differences.

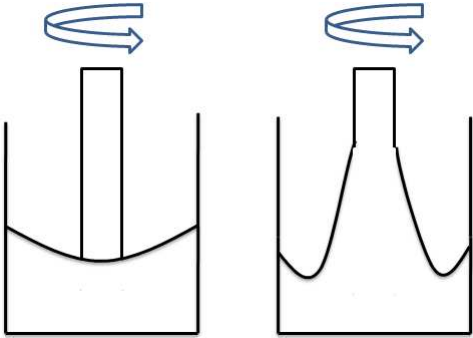


Figure 4.2: Rod climbing effect

4.5 Previous Rheological Results

This section will present some of the established rheological results and will motivate the focus of this research.

4.5.1 Newtonian liquids

Figure 4.3 below shows a Newtonian liquid subjected to shearing conditions. The shear stress developed will be a linear function of the imposed shear rate. The normal stresses developed will be equal in all directions and equal to the pressure. Therefore normal stress differences will be zero. This is a Newtonian behaviour and the description is complete just with the use of a single viscosity coefficient.

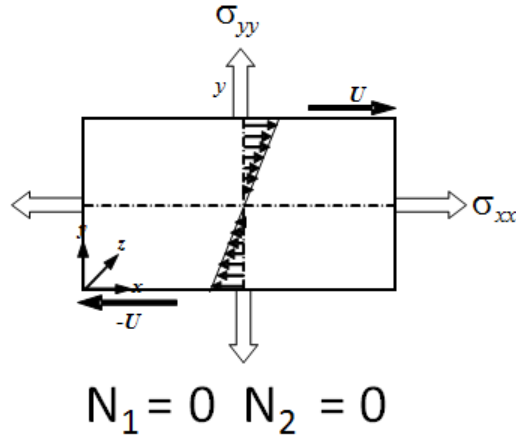


Figure 4.3: Shear rheology for a Newtonian liquid

4.5.2 Emulsion: Stokes flow

Figure 4.4 below shows Newtonian drops dispersed in a Newtonian liquid and the system is subjected to shearing conditions. It has been calculated (Choi-Schowalter model) [8] that the system exhibits shear thinning i.e. viscosity decreases with shear rate. The normal stress differences are non-zero with $N_1 > 0$ and $N_2 < 0$. These results are valid under Stokes flow condition i.e. negligible inertia. The normal stress differences arise because of the stretching of the drops (this will be explained in detail in later sections). This behaviour is called viscoelastic: visco due to the presence of viscosity and elastic due to normal stress differences. This description has also been verified by the simulations of Lowenberg and Hinch [2] and Zinchenko and Davis [17].

4.5.3 Rigid particle suspension

Suspensions have been investigated thoroughly using Stokesian dynamics and experiments. A review of some of the results was presented in the chapter 1 and is repeated here. Stokesian dynamics predicts different behaviour under differing conditions. It predicts shear-thinning and $N_1 > 0$ and $N_2 < 0$ for low Peclet numbers. The behaviour changes to shear-thickening and $N_1 < 0$ and $N_2 < 0$ as the strength of the hydrodynamic forces increase [14]. Zarraga et al. [15] experimentally verified

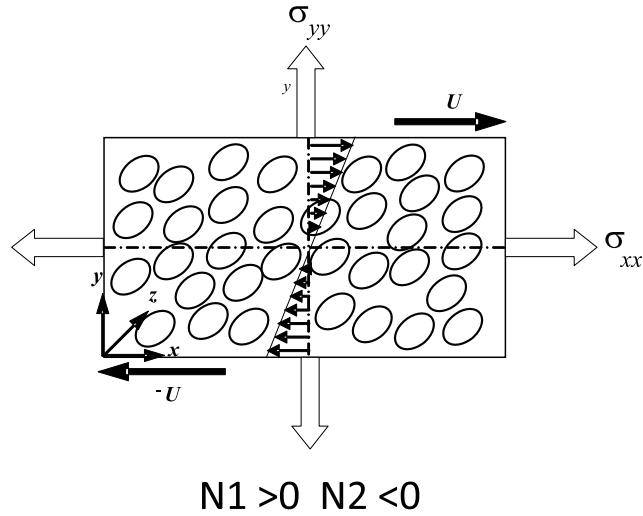


Figure 4.4: Shear rheology for an emulsion under Stokes flow

the presence of non-zero normal stress differences for non-colloidal suspensions (under Stokes flow condition) with $N_1 < 0$ and $N_2 < 0$. The presence of non-zero normal stress differences for rigid particle suspensions is explained by the asymmetry in the micro-structure by the use of pair-distribution function.

4.5.4 Dilute emulsion: Finite inertia

Li and Sarkar [21] using numerical simulations showed that increasing inertia results in the reversal of the signs of normal stress differences. The study was for a dilute emulsion using a single drop. This qualitative behaviour was also verified by the subsequent perturbative analysis of Raja et al. [22].

The current research investigates finite inertia effects in a concentrated emulsion consisting of multiple drops.

Chapter 5

STEADY SHEAR RHEOLOGICAL RESULTS

The previous few chapters served to describe the problem and the different ideas used for studying the rheology of a complex liquid like emulsion. This chapter will present the main results of this thesis. After showing the validation of the code and tuning the parameters for an accurate prediction of rheology, the main results will be discussed. A physical insight into the behaviour of the emulsion under shearing condition will also be provided as an explanation of the results. The problem set-

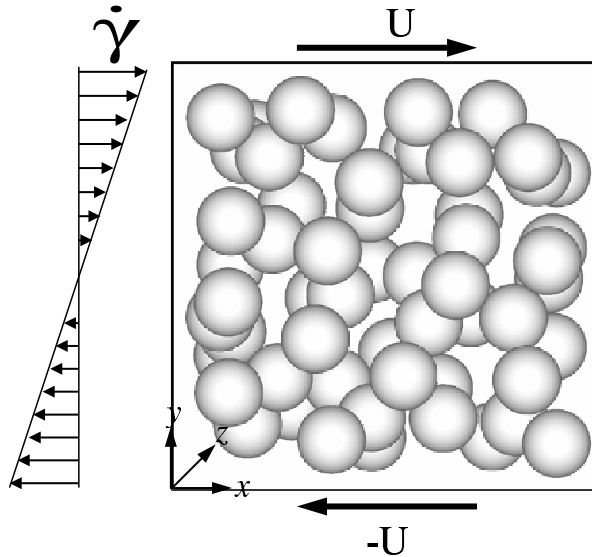


Figure 5.1: Schematic diagram showing the computational domain

up is recapitulated and is shown in figure 5.1. The shear flow velocity direction is demarcated as the X-axis, the velocity gradient as the Y-axis and the vorticity as the Z-axis. The top and the bottom Y walls (parallel to x-z plane) move with a $+U$ and $-U$ velocity, respectively, so as to create uniform velocity gradient of $\dot{\gamma}$. The boundary

conditions at these Y walls are that of no slip condition and at the X and Z walls are of periodic nature. Inside this domain multiple drops are positioned randomly with an initial velocity distribution of uniform steady shear. Using the simulations from the front tracking code, effective properties are calculated by employing the rheological concepts that were outlined in the previous chapter.

5.1 Validation

The code was first validated by considering a dilute emulsion of volume fraction of 0.25% and comparing the results with the predictions of Choi-Schowalter (C-S) model [8]. As this is a Stokes flow model, the Reynolds number for the simulations was kept at a low value of 0.1. The dilute emulsion consists of four drops initially positioned at random locations. The size of the domain was fixed as $l \times 2l \times l$ ($l/a = 15$) and the grid resolution is $128 \times 256 \times 128$. These parameters were adjusted to get a good match with the theoretical values. Figure 5.2 shows the comparison of the normal stress differences and the inset of the figure compares the shear stress. The stresses have been scaled by $\mu\dot{\gamma}\phi$. The normal stress differences match is quite good and the shear stress match well at the low capillary numbers. At higher Ca, the curves show deviation and this is expected because the C-S model is valid under small deformation of the drops and at higher Ca the drops deformation violate the assumption of this model. These comparisons confirm the ability of the code to predict the rheology of emulsions.

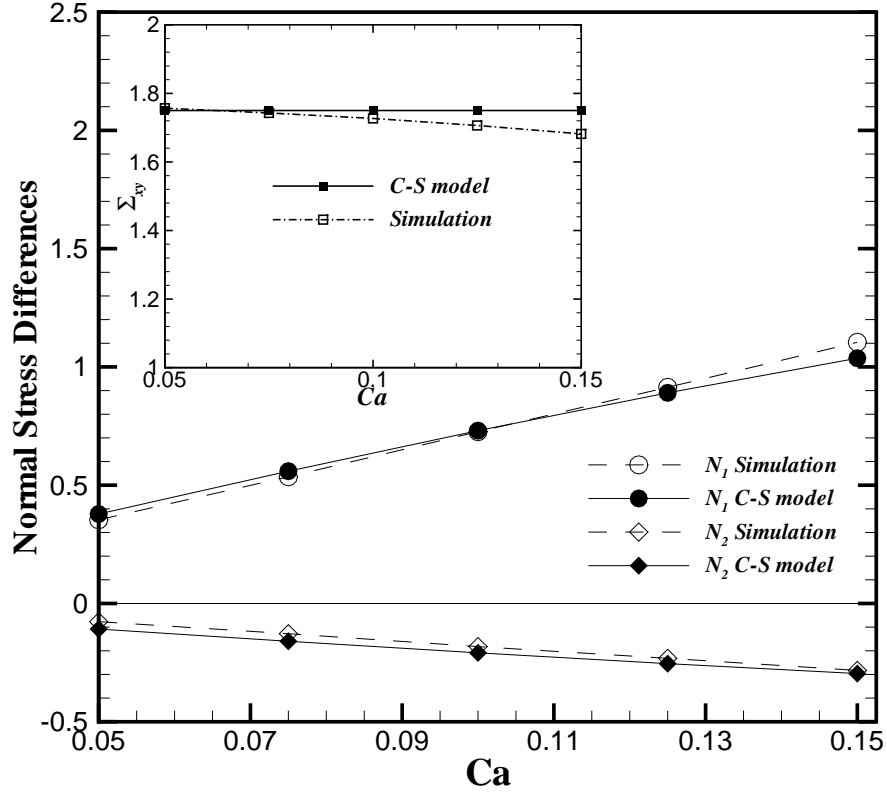


Figure 5.2: Comparison of the simulation and C-S model. The stresses are scaled by $\mu\dot{\gamma}\phi$

5.2 Concentrated Emulsion

We investigated the rheology of emulsions at varying capillary numbers and inertia in the volume fraction range of: 5-27%. Accurate rheological predictions can be made by first studying the sensitivity of the results on the grid resolution, number of drops, their size relative to domain and their initial position. This is discussed in detail in the following section. The data that will be reported in the tables and figures in the later sections invoke time averaging. The curves for the interfacial stresses show a lot of fluctuation as they involve multiple drop interactions, which will continue to occur throughout the simulations. To give a good estimate of the data, the statistical

uncertainties associated with it also needs to be considered. Figures 5.3- 5.5 below show the plots for the evolution of the interfacial stresses with the non-dimensional time. The fluctuating behaviour of these data is evident. The method used for determining the mean values for all the simulations is this: First of all, an initial transient part of the simulation is discarded. This is done by looking at the curves and most of the time this developing part is evident. After discarding that portion, the remaining parts of the curves are divided into subdivisions of 30-40 time units. In each of the subdivisions, the average is calculated and the mean of these averages are reported as the time averaged data (or rather ensemble averaged if the system is ergodic). The standard deviation of the different averages are reported as the error bars. This ensures that the separate average values are approximately uncorrelated values. Most of the simulations are run upto 200-300 time units.

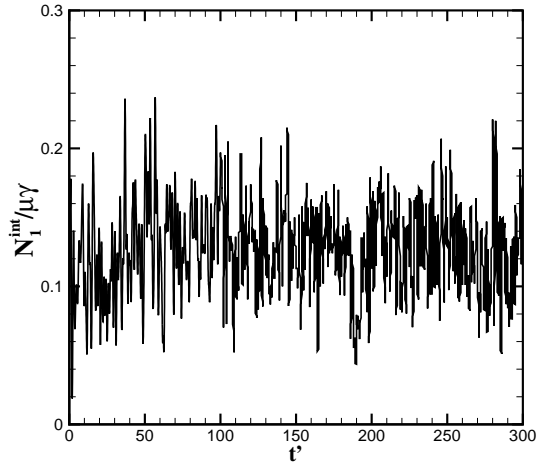


Figure 5.3: Time variation of N_1^{int}

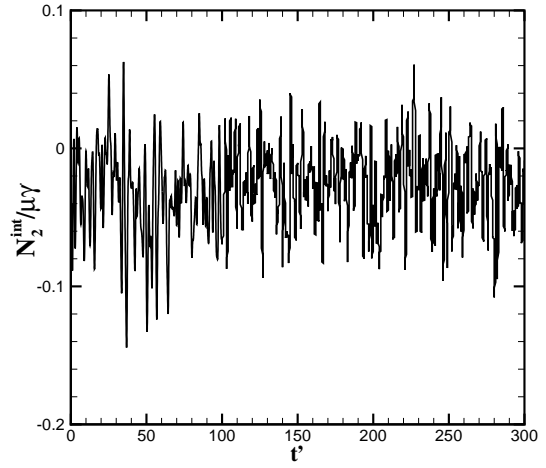


Figure 5.4: Time variation of N_2^{int}

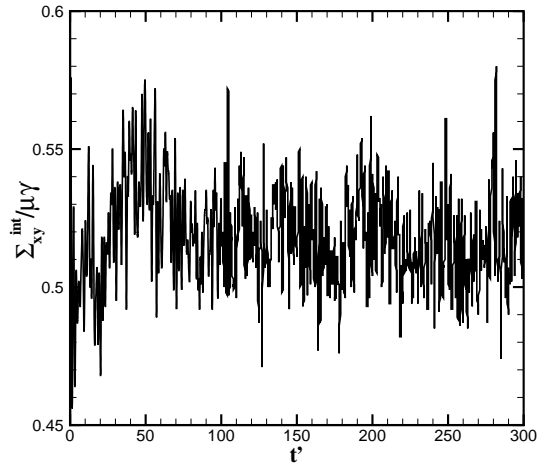


Figure 5.5: Time variation of Σ_{xy}^{int}

5.3 Grid Resolution

Front Tracking method has two grids. The first mesh is a Cartesian fixed mesh, and the second is a moving surface mesh. The resolution of the fixed mesh affects the calculations of Navier Stokes equations. It also determines how well the drops are resolved to accurately capture their morphology. The surface mesh is composed of triangular elements and its resolution is important to accurately calculate the surface tension forces. The surface mesh involves adaptive regridding and the number of elements it contains keeps on changing as was described briefly in the previous chapter. The initial number of elements that are present on each drop is a squared function of the ratio of drop's radius and fixed mesh spacing.

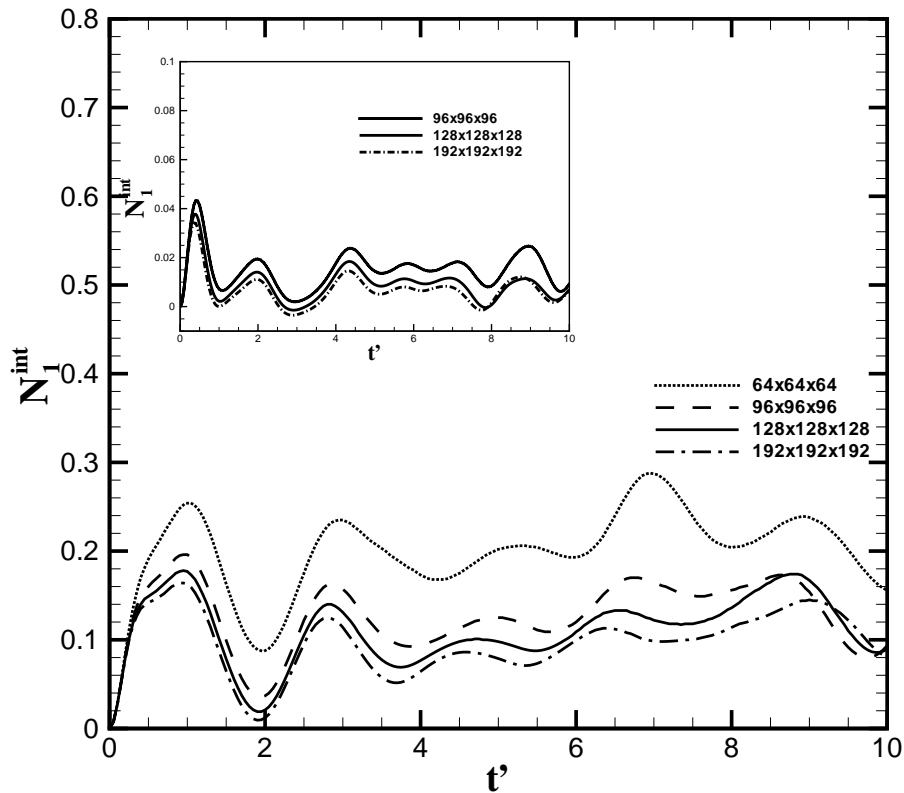


Figure 5.6: Grid resolution test for N_1

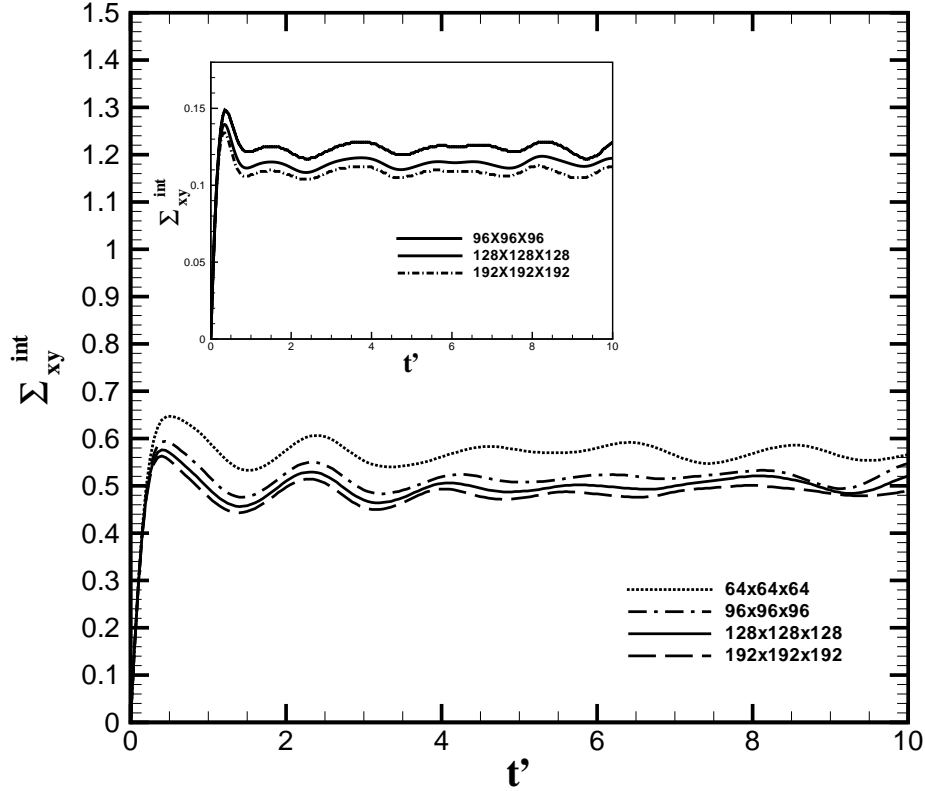


Figure 5.7: Grid resolution test for Σ_{xy}

Figure 5.6 and 5.7 show the grid resolution tests for volume fractions of $\phi = 20\%$ and $\phi = 0.05\%$ respectively. The simulations were run on grid resolutions of $64 \times 64 \times 64$, $98 \times 98 \times 98$, $128 \times 128 \times 128$ and $192 \times 192 \times 192$. The drop number was fixed at 64, Ca at 0.05 and Re at 1.0. The main plot shows the curves for $\phi = 20\%$ and the insets in the plots are for $\phi = 5\%$. The plots are just a snapshot of the results for the first 10 time units. The entire range of data is avoided for clarity, however the average values (time average) reported in the tables below are obtained by running simulations upto 200-300 strains.

The data in tables 5.1, 5.2, 5.3 are taken by the method outlined before. The results in table 5.1 show that normal stress differences show more sensitivity to the grid

Table 5.1: Table showing the grid resolution test for $\phi = 20\%$, $\text{Re}=1.0$ and $\text{Ca}=0.05$

Grid resolution	$N_1(\times 1E - 01)$	$N_2(\times 1E - 02)$	$\Sigma_{xy}(\times 1E - 01)$	Deformation ($\times 1E - 01$)
64x64x64	2.21 ± 0.0547	-6.74 ± 0.4711	6.06 ± 0.00481	1.20 ± 0.0307
96x96x96	1.54 ± 0.103	-4.96 ± 0.706	5.59 ± 0.00358	1.11 ± 0.0099
128x128x128	1.33 ± 0.0433	-3.22 ± 0.851	5.23 ± 0.00702	9.96 ± 0.0262
192X192X192	1.17 ± 0.0916	-3.13 ± 0.502	5.19 ± 0.00223	9.89 ± 0.0205

Table 5.2: Table showing the grid resolution test for $\phi = 20\%$, $\text{Re}=1.0$ and $\text{Ca}=0.20$ (average values only)

Grid resolution	$N_1(\times 1E - 01)$	$N_2(\times 1E - 01)$	$\Sigma_{xy}(\times 1E - 01)$
128x128x128	5.12	-1.29	4.11
192x192x192	4.90	-1.23	4.02

resolution while the shear stresses and deformations are more robust. The normal stress differences at the low Ca of 0.05 are small quantities and therefore are more difficult to capture accurately. For $\text{Ca}= 0.20$ the normal stresses are of larger magnitude and show much less sensitivity to grid resolution as suggested by table 5.2. The lesser volume fraction case of 5% is more difficult because at lower volume fractions the drops sizes are smaller and finer grids are needed to resolve the drops accurately. Along with this the small magnitude of the stresses compounds the difficulty. The above two-volume fraction cover the range in which we want to operate. The grid resolution of $128 \times 128 \times 128$ gives satisfactory convergence especially for the higher volume fraction and is fixed for the entire study considering the accuracy of the results and the time limitations for running the simulations.

Table 5.3: Table showing the grid resolution study for $\phi = 0.05\%$, $\text{Re}=1.0$ and $\text{Ca}=0.05$

Grid resolution	$N_1(\times 1E - 02)$	$N_2(\times 1E - 03)$	$\Sigma_{xy}(\times 1E - 01)$	Deformation ($\times 1E - 02$)
96x96x96	1.67 ± 0.0654	4.63 ± 0.517	1.21 ± 0.00589	8.32 ± 0.0872
128x128x128	1.07 ± 0.0265	6.04 ± 0.232	1.11 ± 0.00755	7.58 ± 0.0821
192x192X192	0.760 ± 0.0442	7.06 ± 0.442	1.06 ± 0.00336	7.05 ± 0.0807

5.4 Drop Number Dependence

The number of drops used for simulating the flow can affect the calculated rheology. Zinchenko and Davis [17] studied how the number of drops used for rheology calculation can be a source of both systematic and statistical errors. The statistical errors arise due to finite time averaging and can be decreased by averaging over longer time units so that sufficient non-correlated drops interactions are captured. However, the systematic errors may persist due to finite domain size (periodic boundary conditions) and especially due to the presence of walls.

The presence of a wall creates additional physical complexities. They result in the migration of drops towards the domain centerline and this has been carefully studied and understood theoretically, experimentally and numerically [43, 44]. Silbilo et al. [45] did a careful study of the single drop deformation and breakup in confined domains. They found that confinement enhances drop deformations and stabilizes large deformed drops, which would otherwise break in non-confined flows. Janssen et al. [46] studied the drop deformation and orientation changes with confinement using boundary integral simulations. These studies were however focused on the cases where the drop radius was comparable to the domain size and so completely new physics was observed. The aim of the present study is to predict free shear properties and so wall effects should be minimal.

When sufficient number of drops are considered, the rheological properties should show less variation with further increase in drops. It should also be noted that considering larger number of drops ensures that their size relative to the wall separation is less and thus the wall effects are minimal. Therefore considering large number of drops for predicting the rheology is essential, though it adds to the computational costs. Table 5.4 shows the dependence of the interfacial and Reynolds stresses on the number of drops for a low capillary number of 0.05 and a Reynolds number of 1.0. This table shows that 16 drops $\approx O(10)$ would predict a significantly higher N_1 and lower shear. The mean values of the stresses show less variation as the drops number is increased beyond 32. The ratio of l/a (i.e. wall separation to drop radius) varies between 7-13

(approximately) for the 16-100 drops range. This table suggests that 64 drops should be sufficient.

Table 5.4: Table showing the drop's number study for $\phi = 20\%$, $Re=1.0$ and $Ca=0.05$

Drops	$N_1(\times 1E - 01)$	$N_2(\times 1E - 02)$	$\Sigma_{xy}(\times 1E - 01)$	$R_{xx}(\times 1E - 02)$	$R_{yy}(\times 1E - 02)$
16	1.57 ± 0.22	-2.74 ± 1.1	4.795 ± 0.068	5.64	2.34
32	1.370 ± 0.089	-2.64 ± 0.37	5.097 ± 0.08	6.48	2.76
64	1.33 ± 0.0433	-3.22 ± 0.851	5.23 ± 0.00702	6.26	2.91
100	1.2564 ± 0.11	-2.997 ± 0.71	5.264 ± 0.099	6.15	3.09

Using 64 drops gives a l/a ratio of around 11. Fixing the number of drops as 64, the wall separation was doubled to get a higher l/a ratio of 18. This was done to further verify that the wall effects are minimal. The results are presented in table 5.5. Even after doubling the wall separation to get a higher l/a ratio the changes in the stresses are quite less. It is somewhat significant for N_2 but this maybe because N_2 itself is too small to be accurately computed. Therefore these two tables suggests that 64 drops (giving a l/a ratio of 11) should be adequate for the prediction of the rheology for $\phi = 0.20\%$.

Table 5.5: Table showing relative domain size influence for $\phi = 20\%$, $Re=1.0$ and $Ca=0.05$

Domain size	$N_1(\times 1E - 01)$	$N_2(\times 1E - 02)$	$\Sigma_{xy}(\times 1E - 01)$	$R_{xx}(\times 1E - 02)$
1x1x1	1.33 ± 0.0433	-3.22 ± 0.851	5.23 ± 0.00702	6.26
1x2x1	1.17 ± 0.0602	-1.87 ± 0.371	5.10 ± 0.00616	6.92

Finally tables 5.6, 5.7 and 5.8 further justify the choice of the number of drops by showing the dependence of the stresses at $Ca=0.20$ ($Re=1.0$) and $Re=5.0$ ($Ca=0.05$) for $\phi = 0.20\%$ and at $Re=1.0$ ($Ca=0.05$) for a lower volume fraction of $\phi = 5\%$ respectively.

Table 5.6: Table showing the drop’s number study for $\phi = 20\%$, $\text{Re}=1.0$ and $\text{Ca}=0.20$

Drops	$N_1(\times 1E - 01)$	$N_2(\times 1E - 01)$	$\Sigma_{xy}(\times 1E - 01)$
64	5.12 ± 0.0562	-1.29 ± 0.0662	4.11 ± 0.0106
100	5.40 ± 0.0405	-1.41 ± 0.0244	4.21 ± 0.0146

Table 5.7: Table showing the drop’s number study for $\phi = 20\%$, $\text{Re}=5.0$ and $\text{Ca}=0.05$ (average values only)

Drops	$N_1(\times 1E - 02)$	$N_2(\times 1E - 02)$	$\Sigma_{xy}(\times 1E - 01)$
64	-2.02	7.63	6.60
100	-2.01	7.43	6.73

Table 5.8: Table showing the drop’s number study for $\phi = 0.05\%$, $\text{Re}=1.0$ and $\text{Ca}=0.05$ (average values only)

Drops	$N_1(\times 1E - 02)$	$N_2(\times 1E - 03)$	$\Sigma_{xy}(\times 1E - 01)$
16	0.9647	6.60	1.04
32	0.922	6.34	1.07
64	1.07	6.04	1.1

5.5 Initial Position

The rheology estimated should be independent of their initial positions. However, choosing an initially random positioning of the drops is important to reduce the time it takes for the system to forget about its past history. This was investigated by fixing the volume fraction, Reynolds number and capillary number while varying the initial positions. Figure 5.8 compares the time evolution of the shear stress for two cases. The first case corresponds to an initial ordered positioning of the drops and the second case corresponds to an initial random positioning. It is clear that the ordered system takes a large amount of time to break the structure. During the initial 70 time units the drops move in layers (which is how they are initially distributed) for the

ordered case. The shear stress is considerably low since the drop-drop interactions are minimal. After the structure breaks, inter drop interactions results in shear stresses close to those obtained from the second case. Therefore this illustrates two points: first of all, the stresses are independent of the initial configuration (which is expected). Secondly, the initial positioning of the drops should be random to get good time-averaged quantities in a reasonable number of cycles. So, for all the simulations, the drops are initially randomly positioned.

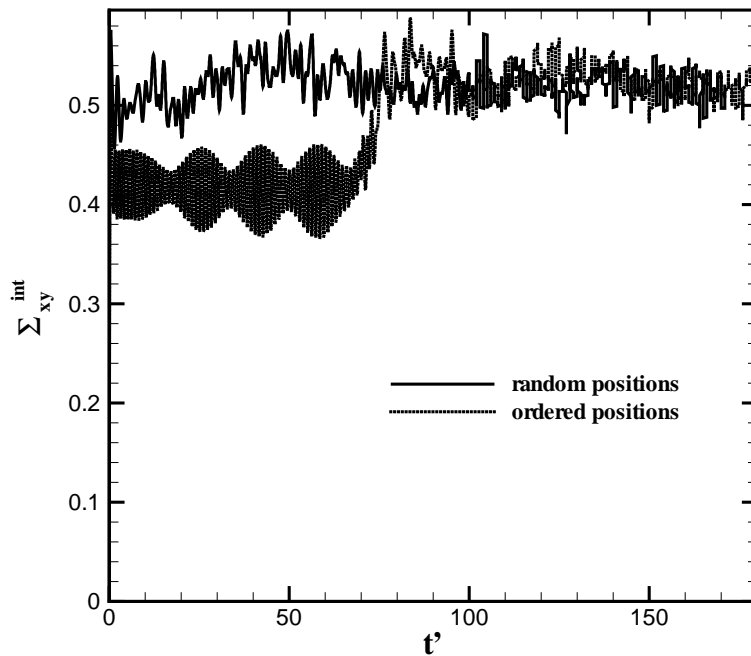


Figure 5.8: Influence of the initial drops' positions

5.6 Comparisons with Numerical Results

After fixing the main parameters of the problem, we first compare our results with some of the existing concentrated emulsion results. Using boundary element methods, Lowenberg and Hinch [2] and Zinchenko and Davis [17] estimated the rheology of concentrated emulsion and we aim to compare our results with them. Figure 5.9 shows a comparison of our results with that of Lowenberg and Hinch. This is for a

volume fraction of 20%. The Reynolds number is fixed at 1.0. The stresses have been scaled with $\frac{\sigma}{a\phi}$. Figure 5.10 shows the comparisons of the results with that of Zinchenko and Davis. The volume fraction is 30% and the Reynolds number is kept at 1.0. For this case, the stresses have been scaled with $\mu\dot{\gamma}$. The scaling of the stresses for both the comparisons have been done according to the respective papers.

The comparisons of the viscosity with that of Zinchenko et al. (figure 5.10) is quite good and the differences lie within 5%. For N_1 they lie within a range of 10% for all the capillary numbers except 0.20. At that Ca it increases upto 20%. The differences between N_2 is not very apparent from the figure but for the lowest Ca of 0.0375 the difference shoots up to 35%. This may be because at this low value of Ca, N_2 is too small to capture it accurately. However, the main reason for the differences should be finite inertial effects. The results of both Loewenberg et al. [2] and Zinchenko et al. [17] were at Stokes flow while the present simulations are at a finite Re of 1.0. Running simulations at smaller Reynolds numbers can be very restrictive due to viscous time stepping restrictions. Figure 5.9 shows the comparisons with Lowenberg and Hinch [2]. The differences for the shear stress in this case remains roughly within 10% range. For N_1 and N_2 they lie within this range for all capillary numbers except 0.20. At this values the N_1 predicted from simulations is roughly 20% lower and N_2 is 25% higher. This again is largely due to the inertial effects, since it will be seen later that increasing inertia causes N_1 to decrease and N_2 to increase respectively. Another source of differences may be the relatively smaller number of drops used for simulations by Lowenberg and Hinch.

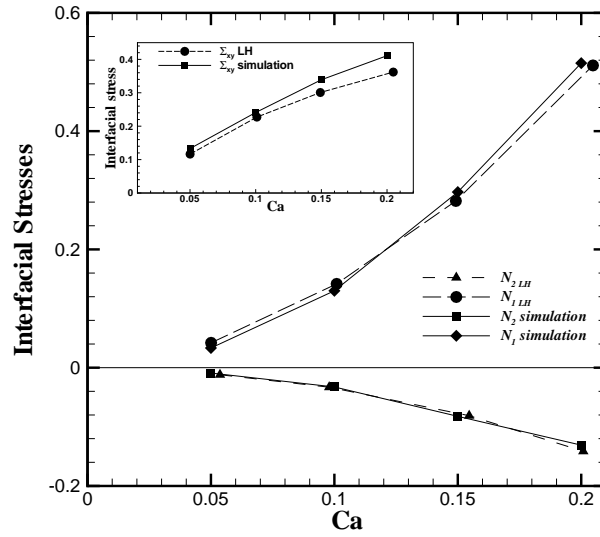


Figure 5.9: Comparisons of interfacial stress with the simulations of Lowenberg and Hinch ($\phi=20\%$)

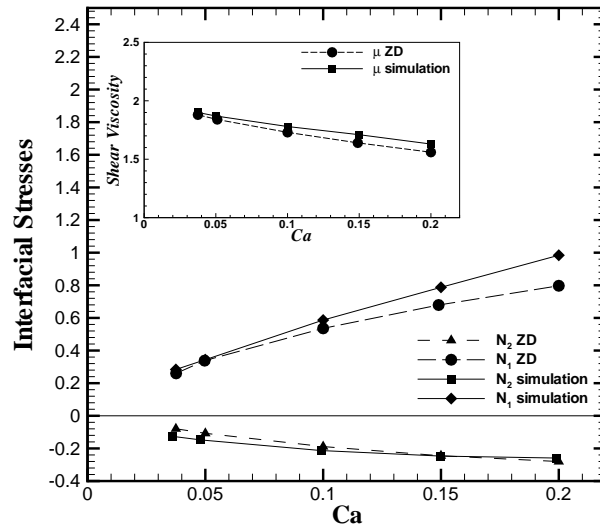


Figure 5.10: Comparisons of interfacial stress with the simulations of Zinchenko and Davis ($\phi=30\%$)

5.7 Dependence of the Interfacial Stresses on Reynolds Number

Figure 5.11 - 5.13 show the dependence of the interfacial stresses with Reynolds number for 4 different volume fractions: 5%, 10%, 20%, 27%. The plots also include the dilute emulsion results of Li and Sarkar [21] where the sign reversal of the normal stress differences with Reynolds number was first noticed. The stresses have been scaled by ϕ to allow comparisons between different volume fractions. The capillary number was fixed at 0.05. Error bars (dashed lines) have also been shown only for interfacial N_1 for volume fraction of 20%. These bars correspond to the statistical fluctuations of the data and the purpose of this is to show that the deviations in the results due to finite time averaging is quite less compared to the changes due to inertia and volume fraction. Similar trends are seen for N_2 and shear stress, and all the remaining error bars are therefore avoided.

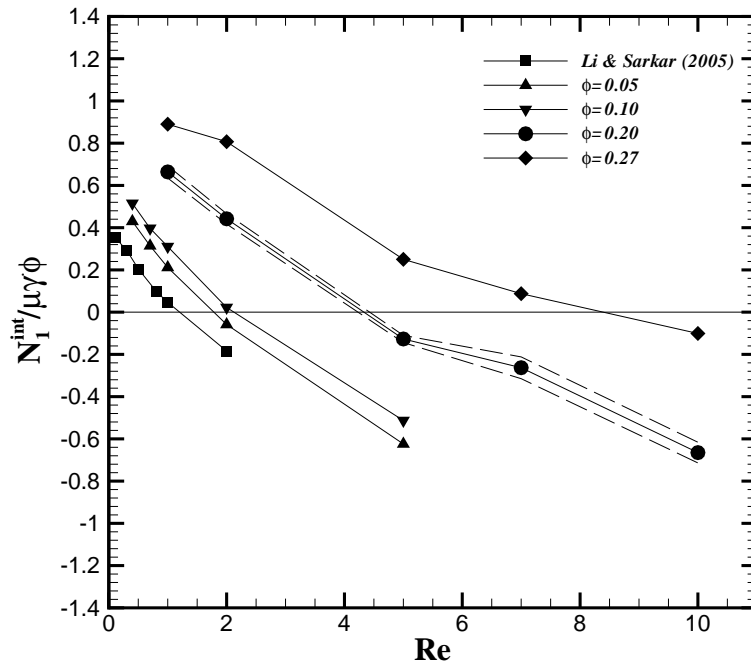


Figure 5.11: Variation of N_1^{int} with Re and ϕ at Ca=0.05

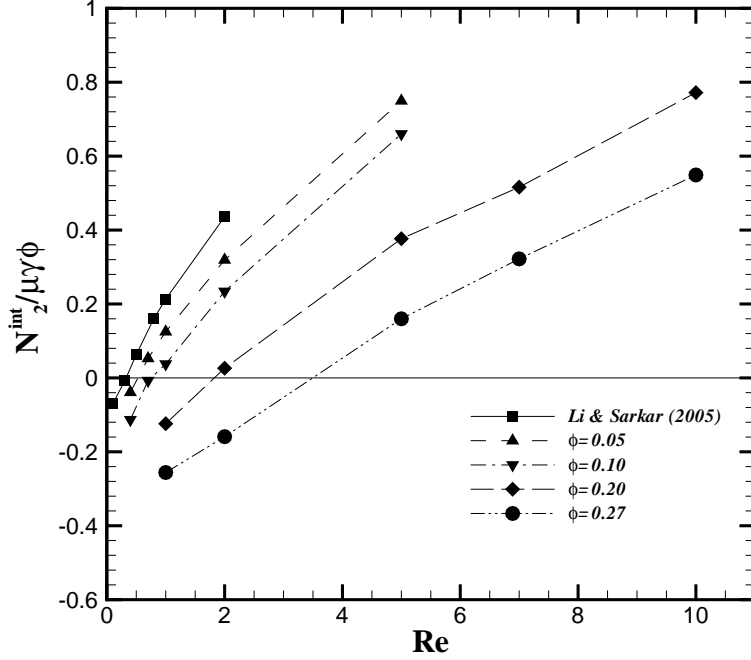


Figure 5.12: Variation of N_2^{int} with Re and ϕ at Ca=0.05

These plots show that the interfacial N_1 and N_2 decrease and increase with Reynolds number respectively for the entire range of volume fraction considered. The curves for different volume fractions do not overlap as the concentration is increased. This indicates that the effect of increasing ϕ is not merely a case of superposition of single drop results. It involves inter-particle interactions which can be pairing, tripling and higher-order interactions (Zhou and Pozrikidis [16]). Increasing volume fraction delays the reversal of the signs of the interfacial normal stress differences. The interfacial shear stress increases with Reynolds number over the volume fraction range considered.

The above observations can be explained by considering the average drops orientations and deformations. Before showing their plots, the connection between the orientation of a drop to the interfacial normal stress differences is explained. This helps

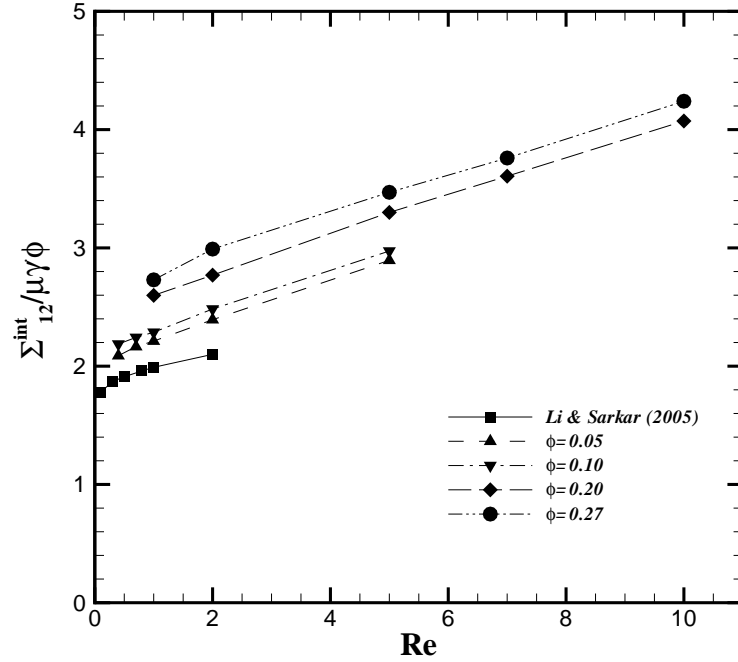


Figure 5.13: Variation of Σ_{xy}^{int} with Re and ϕ at Ca=0.05

in forming a mental picture as how the orientation of drop changes the interfacial normal stress differences. The expression for the first and second normal stress difference goes as:

$$N_1 \sim - \int_{\delta A} (n_x^2 - n_y^2) dA \quad (5.1)$$

$$N_2 \sim - \int_{\delta A} (n_y^2 - n_z^2) dA \quad (5.2)$$

Figure 5.14 shows different orientations of a drop relative to the flow direction. If the drop is aligned along the flow direction then the normals will be oriented more along the velocity gradient direction and this means that $n_x \ll n_y$. From the expressions

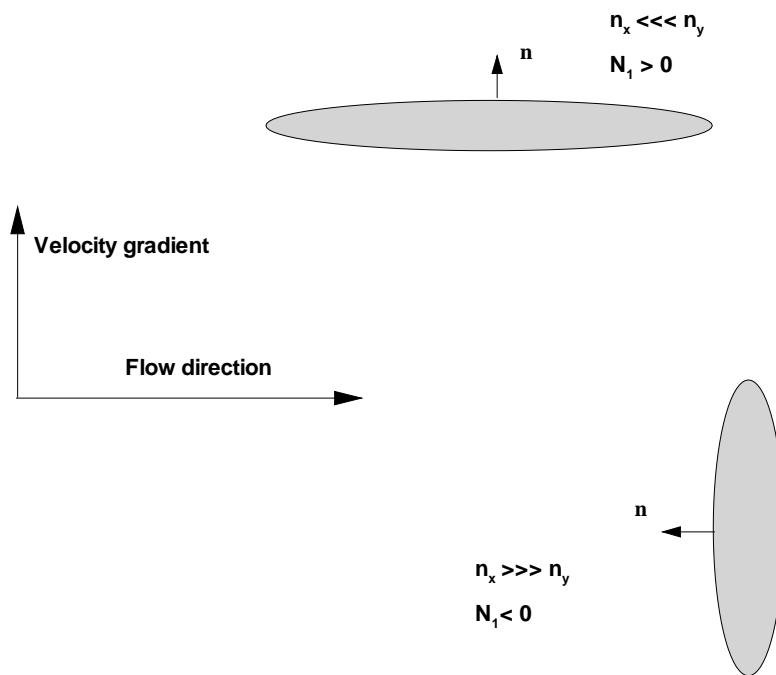


Figure 5.14: Connection between orientation and normal stress differences

of N_1 in equation 5.2 it can be inferred that $N_1 > 0$. The second case is that of the drop aligned along the velocity gradient direction and in this case it is easy to see that $N_1 < 0$. The third case is when the drop is aligned along the 45° line i.e. the extensional axis. This should result in $N_1 \approx 0$. These arguments will be exactly true when the drop shape is ellipsoidal with the shape symmetric about the major axis (or major axis plane). This holds for a single drop in a shear flow, but the above arguments will still hold approximately if the shape is not perfectly symmetrical about the major axis plane, which is the case when drops are interacting. So the conclusion that should be drawn is that if a drop is oriented between the extensional axis and the flow direction, N_1 should be positive, and negative when it is oriented between the extensional axis and the velocity gradient direction. A similar argument can also be given for N_2 . As the drop rotates in its shear plane from the flow direction to the velocity gradient direction, n_y decreases but n_z should roughly remain unchanged. Therefore increasing the orientation of the drop should increase N_2 . It is though more difficult to predict (even approximately) when N_2 would change sign. The above facts can also be extended for a multiple particle system since the total interfacial stresses for such a system is just a summation of the interfacial stresses of the individual drops. So a natural way to define the average orientation of the emulsion would be to calculate the orientations of each drop and then take the average over all the drops.

Figure 5.15 shows the variation of the average orientation of the drops with Reynolds number. It should be noted that for a fixed volume fraction, the drops tend to align themselves more along the velocity gradient direction as the inertia is increased. Li and Sarkar [21], and Singh and Sarkar [23] investigated this observation in detail for a single drop problem. The effect of increasing inertia on individual drops is to orient them along the velocity gradient direction by exerting a torque on the drops. As it was explained in the previous paragraph the increase in the orientation of the drop would lead to an increase in N_2 and decrease in N_1 . Another fact that should be noted is that the orientation of the drops decreases with increasing volume fraction. This behaviour was also noted by Lowenberg and Hinch [2]. Therefore the reason for the delay in the

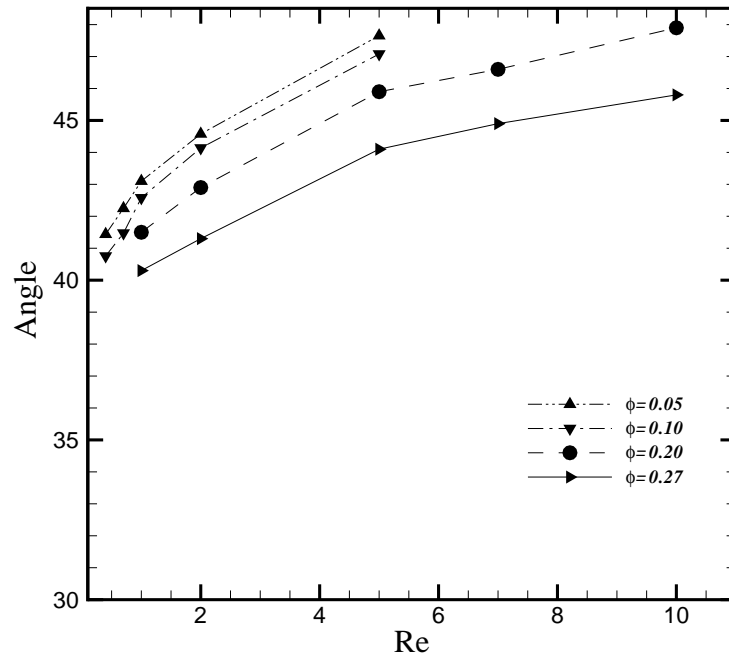


Figure 5.15: Variation of the average orientation with Re and ϕ ($Ca=0.05$)

reversal of the signs of the interfacial normal stress differences with increase in volume fraction can be intuitively understood now.

Figure 5.17 shows the average drops' deformation variation with Reynolds number. The deformation of a single drop is the Taylor deformation parameter shown in figure 5.16 and the average of this value over all the drops gives the deformation of the emulsion. This parameter should be zero when the drops are completely spherical and therefore it is an indicator of the deviation in the shape of drops from the initial spherical geometry. Figure 5.17 show that as the volume fraction is increased the drops are more deformed. The increased deformations are to reduce the obstructions in the trajectory of individual drops.

The explanation of the dependence of shear stress on volume fraction and Re is

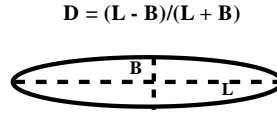


Figure 5.16: Taylor deformation parameter

not completely straightforward. The expression for the shear stress goes as:

$$\Sigma_{xy} \sim - \int_{\delta A} (n_x * n_y) dA \quad (5.3)$$

Referring back to the equation 5.14, it should be noted that if the drop is perfectly aligned along the flow direction or the velocity gradient direction, the shear stress will be very less as its expression involves product of the vectors n_x and n_y . Apart from this it is hard to conclude the changes in the interfacial shear stress when it is oriented at an intermediate angle. So the explanation of the observed shear thickening property cannot be provided simply by considering orientation effects and the deformation effects also need to be included. The expressions for the interfacial stresses for an ellipsoidal-shaped object involves complex elliptic integrals [11]. To circumvent this, a capsule-shaped drop is considered. This is a crude approximation but it explains the shear-thickening behaviour with increasing inertia very well. The shear stress for such a geometry goes as [2]:

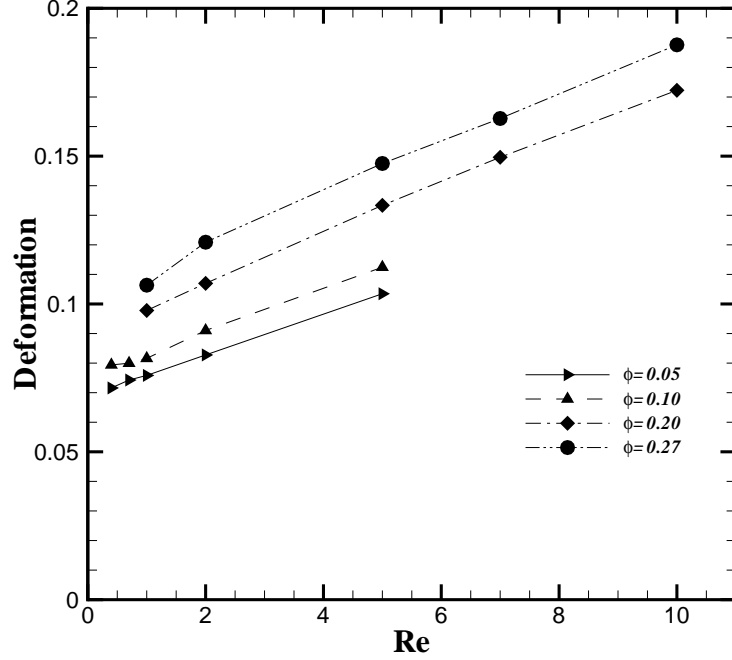


Figure 5.17: Variation of the average deformation with Re and ϕ (Ca=0.05)

$$\Sigma_{xy} \approx \sin(2\theta) * D \quad (5.4)$$

Here D is the Taylor deformation parameter and θ is the orientation of the drop relative to the flow direction. (This approximation is true if the deformation is small, i.e. low capillary number condition.) Due to changes in increasing inertia, orientation and deformation increases. Increasing deformation will increase the shear stress, but increase of the angle beyond 45° should decrease it. So these two effects are opposing in nature. Our average deformation plots show that for an increase of inertia over a range of 1-10, the deformation roughly doubles. The changes in the angle are in the range of a maximum of $\pm 5^\circ$ relative to 45° which means that the $\sin 2\theta$ will reduce from 1 (at 45°) to ~ 0.98 . This change is small compared to the two-fold increase in

the deformation. So the increase in shear stress with inertia and volume fraction is dictated by the increase in deformation. Therefore by considering simple parameters like the average orientation and deformation the observations of figures, 5.11 - 5.13 could be explained.

The effects of inertia on micro-structure is to increase the orientations of the drops as well as their deformation. Increasing deformation tends to induce drop break up. So there should be a limit of Reynolds number range in which the drops are able to sustain the enhanced deformations. This was investigated by Singh and Sarkar [23] in detail for a dilute emulsion (i.e. single drop study). They showed that the combined effect of increasing orientation and deformation leads to the reversal of the signs of the normal stress differences within a particular capillary number range only. This was because higher deformation required a larger torque to increase the orientation of the drop and beyond a certain capillary number the enhanced deformation prevented an increase in orientation. So at high Ca the drop breaks up with a slight increase in Re. They suggested an Ohnesorge dependence of the reversal of signs, which captures the ratio of capillary and Reynolds number.

Figure 5.18- 5.20 capture the dependence of the interfacial normal stress differences and shear stress with inertia over a range of capillary numbers at a fixed volume fraction of 20%. Figure 5.18 shows that the sign change of the interfacial first normal stress difference occurs at a lower Reynolds number for Ca=0.02 as compared to Ca=0.05. The decreasing behaviour of the first normal stress differences with inertia is captured well in the Ca range of 0.02 to 0.075. At Ca of 0.125 and 0.20 the first normal stress difference shows a non-monotonic behaviour. This is because of the fact that for a single drop the sign change of the first normal stress difference is dependent on Ohnesorge number i.e. the ratio of Reynolds and capillary number. Some of the drops begin to break beyond Re=5.0 and Re=2.0 for Ca=0.125 and Ca=0.20 respectively. Similar to the first normal stress difference, the second normal stress difference also shows a delay in the reversal of the signs with increasing capillary number. An empirical relation between interfacial N_1 and shear stress with Reynolds number for

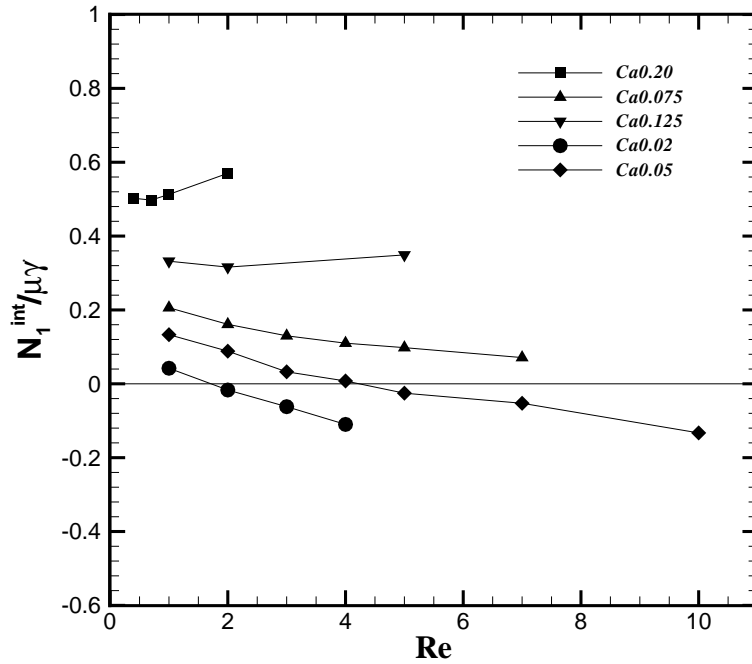


Figure 5.18: N_1^{int} variation with Re over a range of Ca . ($\phi = 20\%$ fixed)

$Ca=0.02$ is also calculated using a linear fit. The relations are:

$$N_1 = -0.0501 * Re + 0.0886$$

$$\Sigma_{xy} = 0.0311 * Re + 0.5458$$

Figure 5.20 shows that interfacial shear stress increases with Reynolds for the entire range of capillary numbers considered. This is a pure manifestation of the enhanced drop deformation with increasing inertia at all the capillary values. It can also be concluded that the system exhibits a shear thinning behaviour with increasing capillary number, which is well known for this type of an emulsion. This is considered in the next section.

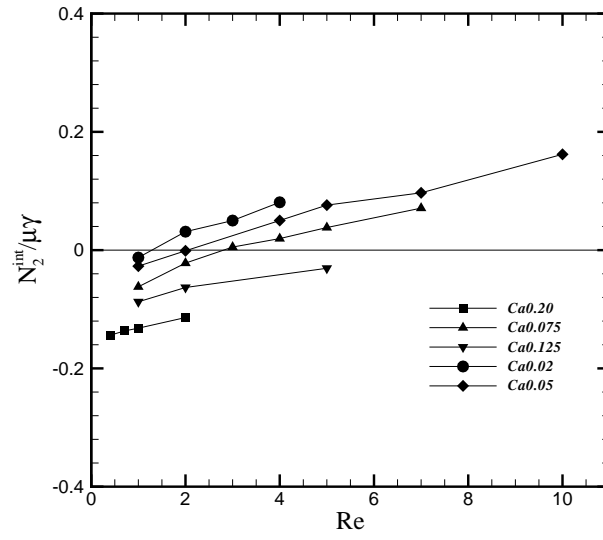


Figure 5.19: N_2^{int} variation with Re over a range of Ca. ($\phi=20\%$ fixed)

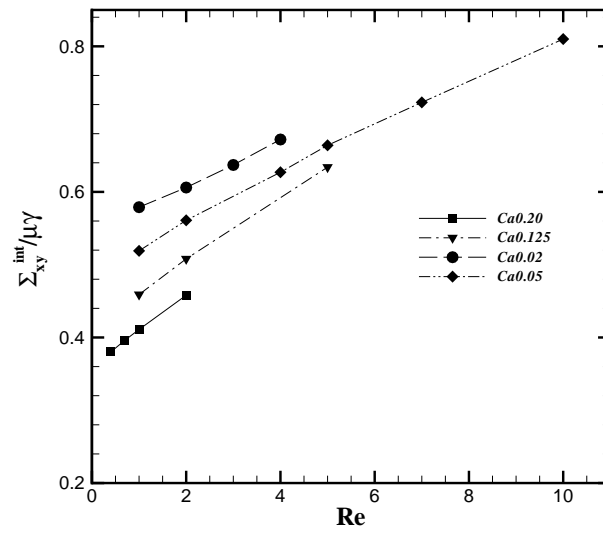


Figure 5.20: Σ_{xy}^{int} variation with Re over a range of Ca. ($\phi=20\%$ fixed)

5.8 Capillary Number Variation

Figure 5.21 and 5.22 show the dependence of the interfacial stresses and the deformation and orientation parameters on the capillary number. The Reynolds number was fixed at 1.0 and the volume fraction at 0.20%. Increasing capillary number results in a shear thinning behaviour, which is a well know fact. The effect of increasing capillary number is to enhance the drop deformation (fig. 8(b)). This is to be expected because increasing capillary number implies the decrease of surface tension forces relative to straining viscous forces. The inset of fig 8(b) shows that the average orientation of the drops is inclined more towards the velocity direction as capillary number is increased. This is also intuitive because larger straining forces at higher capillary number will decrease their orientations. The decreased orientation of the drops is responsible for the large interfacial first normal stress difference and the shearing thinning behaviour. The underlying idea behind this was explained in the previous section by using figure 5.14 and equations 5.2 and 5.3. The shear thinning behaviour and the increase in first normal stress difference was measured experimentally by Han and King [47], and these qualitative behaviours agree with the results of Lowenberg and Hinch [2].

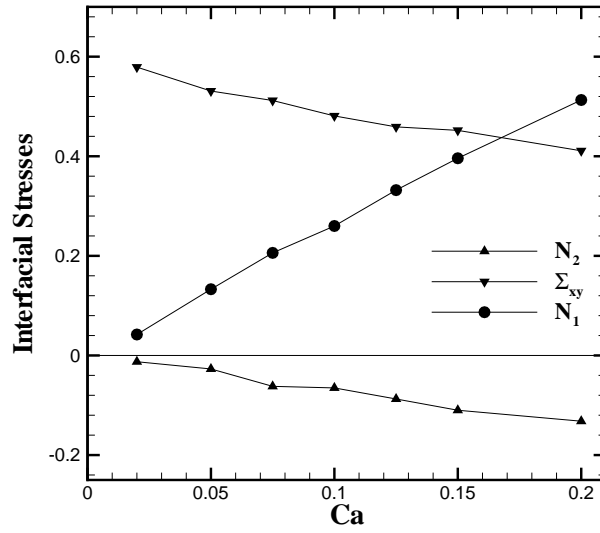


Figure 5.21: Interfacial stresses variation with Ca ($\phi=20\%$, $Re=1.0$)

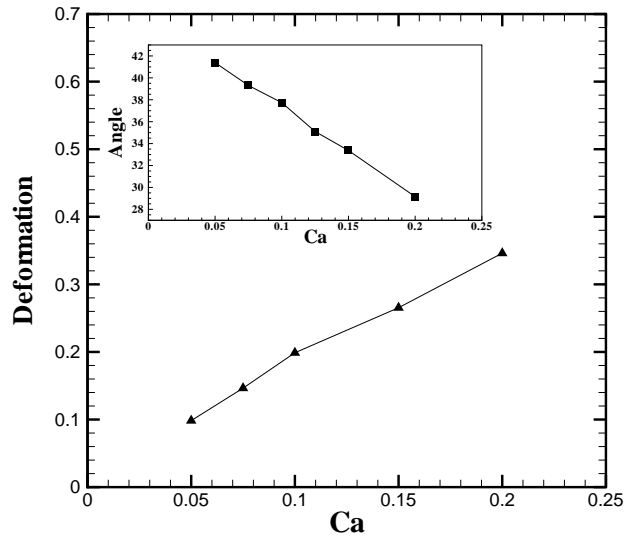


Figure 5.22: Average deformations and orientations variations with Ca ($\phi=20\%$, $Re=1.0$)

5.9 Reynolds Stresses

Figure 5.23 shows the velocity profile of the X-component velocity (flow direction) for $\phi = 20\%$, capillary number of 0.05 and Reynolds number of 10. The velocity has been averaged over x-z plane and over time as well. The velocity has been scaled by the imposed velocity scale and the distance y with the wall separation. There are small perturbations of the averages velocity about the linear velocity field and the velocity remains very close to the linear profile. This type of plot was tried for other range of capillary and Reynolds numbers as well and the resulting velocity distributions were all very similar, just displaying small perturbations about the linear profile. These small disturbances arise from the presence of drops.

Figure 5.24 shows the variation of the drop's center velocity at different locations along the Y direction. To estimate this quantity the y separation was divided into 100 equal sized bins. The drops were put in the respective bins according to their centres' y coordinate. The velocity in each bin was obtained by averaging over the velocity of the different drops that occupied the particular bin during the simulation time. This is a good approximation of the drop's velocity at different positions along the Y direction. Figure 5.24 shows that the drops' average velocity too remains very close to the linear profile and this means that the drops' centres move with the local velocity field. The perturbations that are there in the velocity field are captured by the Reynolds stresses present in the stress formulation and has been discussed briefly in the rheology section.

Figure 5.25 shows the variation of the Reynolds stresses with volume fraction. The figure shows the three components R_{xx} , R_{yy} and R_{zz} . The cross components i.e. R_{xy} , R_{xz} , R_{zy} are relatively much small quantities and they do not influence the total stresses. They are therefore avoided in the plots. The components R_{yy} and R_{zz} show a roughly linear dependence with volume fraction and if the curves are interpolated they will become zero at diminishing volume fraction. However, R_{xx} shows non linear dependence and this is evident from the fact that the curve has to pass through origin. The figure suggests that it shows a somewhat square root dependence on the volume fraction.

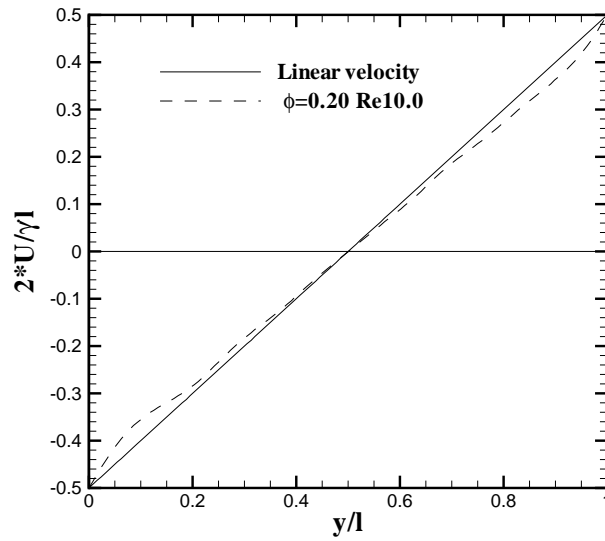


Figure 5.23: Velocity profile $\phi=0.20$, Re_{10} , $Ca_{0.05}$

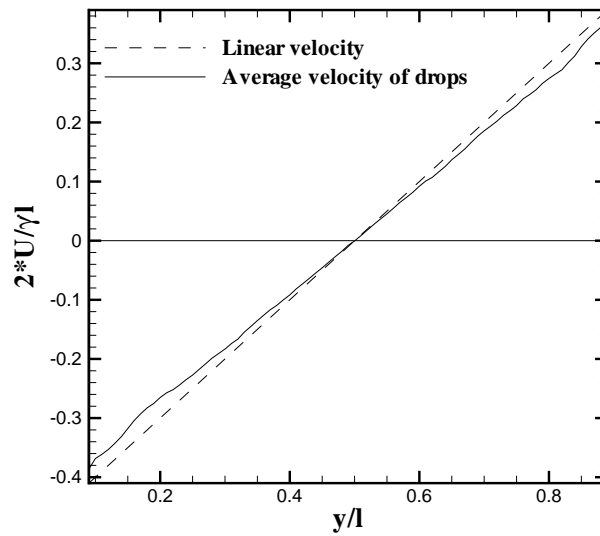


Figure 5.24: Average velocity of drops' centers $\phi=0.20$, Re_1 , $Ca_{0.05}$

Figure 5.26 and 5.27 show the dependence of the Reynolds stresses with Reynolds number at two different Ca (0.020 and 0.075) at a fixed volume fraction of 20%. For

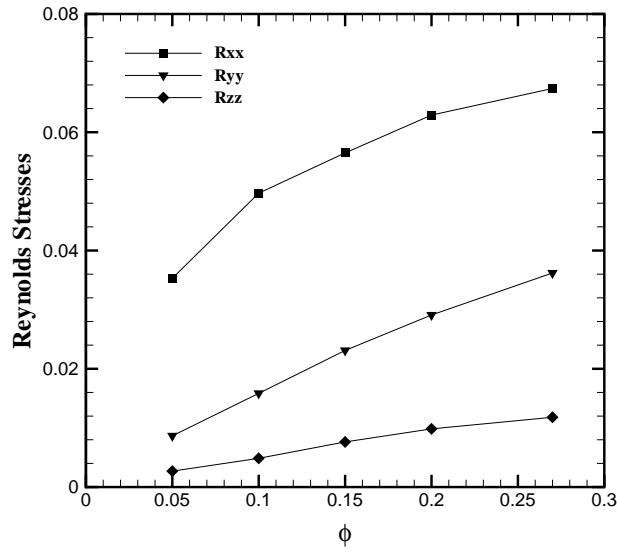


Figure 5.25: Reynolds stresses dependence on ϕ ($Ca=0.05$ and $Re=1.0$)

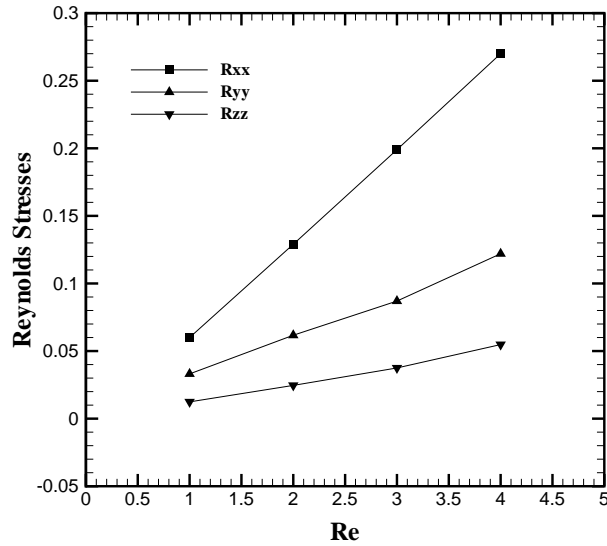


Figure 5.26: Reynolds stresses dependence on Re ($\phi=0.20\%$ and $Ca=0.02$)

$Ca=0.02$, the Reynolds stress scale linearly with Reynolds number in the Re range of 1 to 4. For $Ca=0.075$ the figure indicates that the the R_{xx} component shows a weak

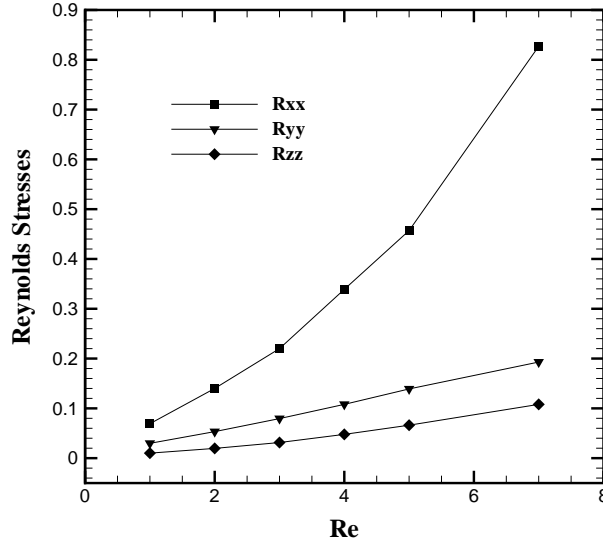


Figure 5.27: Reynolds stresses dependence on Re ($\phi=0.20\%$ and $Ca=0.075$)

non-linear increase with Re while the remaining components show a linear dependence. Figure 5.28 shows the dependence of the differences of the Reynolds stresses (which we call here perturbation stresses) at $Ca=0.05$. This too shows that over a higher Re range the N_1^{ptb} shows a weak non-linear increase with Re and this was also observed by Li and Sarkar [21] for dilute simulations. As the curves indicate, perturbation stresses should vanish at zero Re.

This linear scaling of the Reynolds stresses with Reynolds number (atleast for the low Reynolds numbers) can be explained using simple arguments. The Reynolds stresses have been scaled with $\mu\dot{\gamma}$. The expression for the Reynolds stress goes as $\sigma^{re} \sim \int_V \rho \mathbf{u}' \mathbf{u}' dV$. In the previous plot of the drop's centre velocity (figure 5.24) it was shown that they approximately move with the local velocity field. So the correct scale for the perturbation velocity should be $u' \sim \dot{\gamma}a$. Therefore $\frac{\sigma^{re}}{\mu\dot{\gamma}} \sim Re \int_V \rho \underline{\mathbf{u}}' \underline{\mathbf{u}}' dV$. Here the term $\underline{\mathbf{u}}'$ is the perturbation velocity scaled with $\dot{\gamma}a$.

Figure 5.29 and 5.30 show the time evolution of the Reynolds stresses R_{xx} and R_{yy} for $\phi=20\%$ and $Ca=0.05$. The stresses have been scaled with Reynolds number.

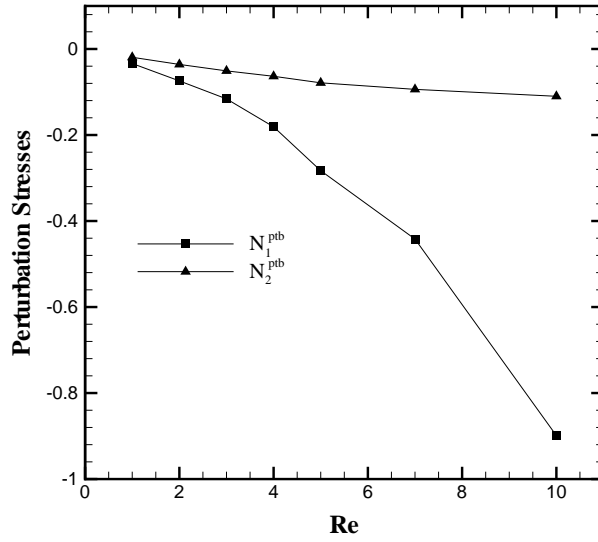


Figure 5.28: Perturbation stresses dependence on Re ($\phi=0.20\%$ and $Ca=0.05$)

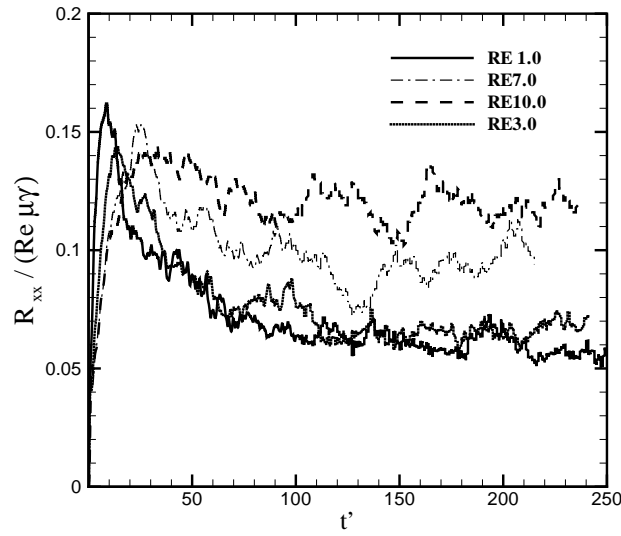


Figure 5.29: Time evolution of R_{xx} for different Re ($\phi=0.20\%$ and $Ca=0.05$)

Figure 5.29 shows that the curves for $Re=1$ and $Re=3$ are very close and this is a manifestation of the linear scaling of the R_{xx} with Reynolds number. The $Re=7$ and 10

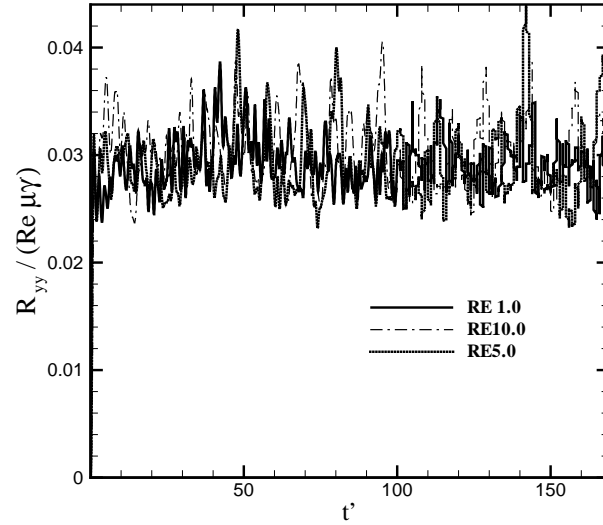


Figure 5.30: Time evolution of R_{yy} for different Re ($\phi=0.20\%$ and $Ca=0.05$)

curves predict higher values which corresponds to the non-linear increase. Figure 5.30 shows that the curves for all the three Reynolds numbers 1,5 and 10 are close to each other and this shows the linear scaling of the R_{yy} component with Reynolds number even upto higher Re . Few more interesting observations can also be made. Figure 5.29 clearly shows that R_{xx} takes certain amount of time to reach a steady value. This is somewhat surprising because it is a volume average quantity and probably it is suggestive of some sort of configuration time-scale. It should also be noted that the lower Reynolds numbers cases take more time to reach a steady value.

Finally fig. 5.31 shows the variation of the Reynolds stresses with capillary number at a fixed Reynolds number of 1.0 and volume fraction of 0.20. Increasing capillary number increases the magnitude of R_{xx} and decreases the magnitude of R_{yy} and R_{zz} . This means that increasing capillary number is increasing the disturbances along the x direction (flow direction). This can be explained by the fact that increasing capillary number orients and deforms the drops more along the x- direction and this increases the disturbances along that axis.

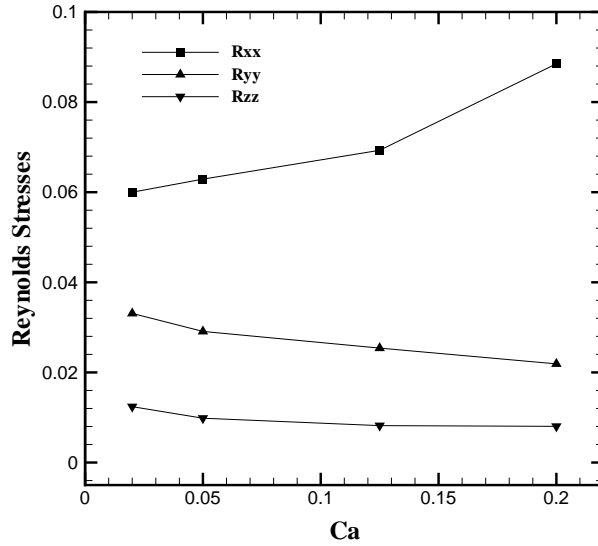


Figure 5.31: Reynolds stresses dependence on Ca ($\phi=0.20\%$ and $Re=1.0$)

5.10 Excess Stresses

The bulk properties of the emulsion or its constitutive relation is captured by the excess stresses which are a combination of both the interfacial and Reynolds stresses. The previous two sections discussed about these two terms individually. Near the Stokes flow condition, the behaviour of the excess stresses are governed by the interfacial terms only as the Reynolds stresses are negligible. Increasing inertia enhances the influence of the Reynolds stresses on the total quantity. This influence is limited to the normal stress differences only as the Reynolds stresses affecting the excess shear stress remain small for the range of Reynolds numbers considered.

$$\sigma^{excess} = \sigma^{int} + \sigma^{re}$$

For a volume fraction of 20-27%, both the stresses influence the excess stress in the Reynolds number range of 2-5 (provided the drops do not break). Beyond that, the behaviour specially for the first normal stress difference is completely dictated by the Reynolds stresses. This occurs from a lower Reynolds number for the lower volume

fractions.

Figure 5.32, 5.33 and 5.34 show the dependence of the excess stresses with Reynolds number. The scaling of the plots are same as that of the interfacial stresses plots. The figures indicate that qualitatively the behaviour of the excess stress plots remain the same as the interfacial stress curves. The addition of the Reynolds stresses make the N_1 curves steeper and they remain negative for most of the Reynolds numbers. This negative sign (with increasing inertia) for N_1 is now contributed by both the interfacial and Reynolds stresses. The addition of the Reynolds stresses to N_2 makes these curves relatively flat. This is because of the opposite behaviour of the interfacial and Reynolds stress component of N_2 with increasing Re . As pointed out earlier, the Reynolds stresses have very little effect on the shear stresses.

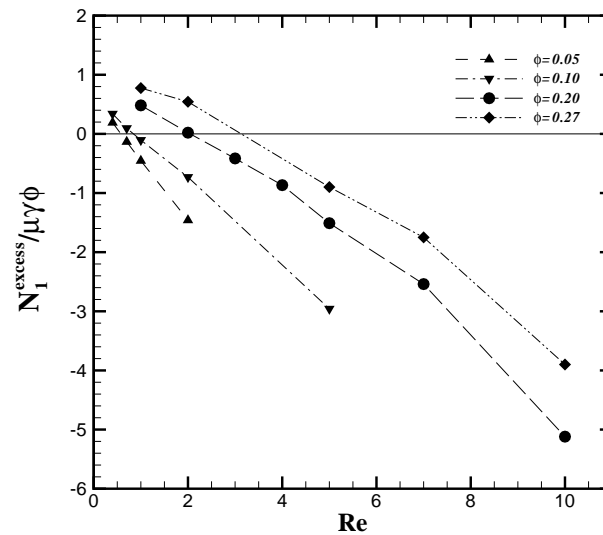


Figure 5.32: N_1^{excess} variation with Re ($Ca=0.05$ fixed)

The significance of the signs of the normal stress differences show up in the cone and plate rheometer. If the rheometer contains a Newtonian liquid, no forces would be felt on the bottom plate. For an emulsion composed of Newtonian drops dispersed in

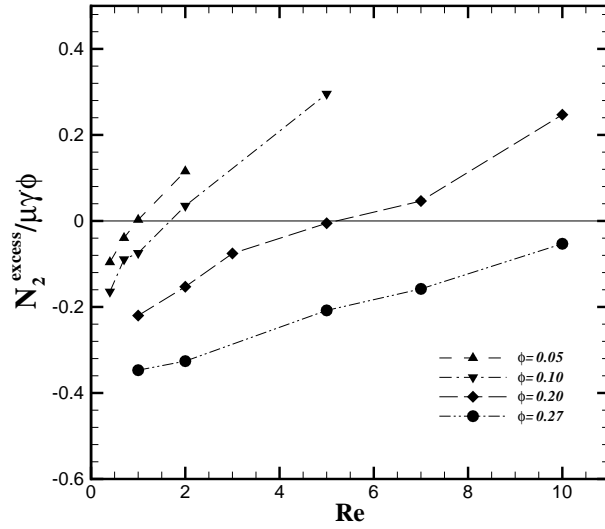


Figure 5.33: N_2^{excess} variation with Re (Ca0.05 fixed)

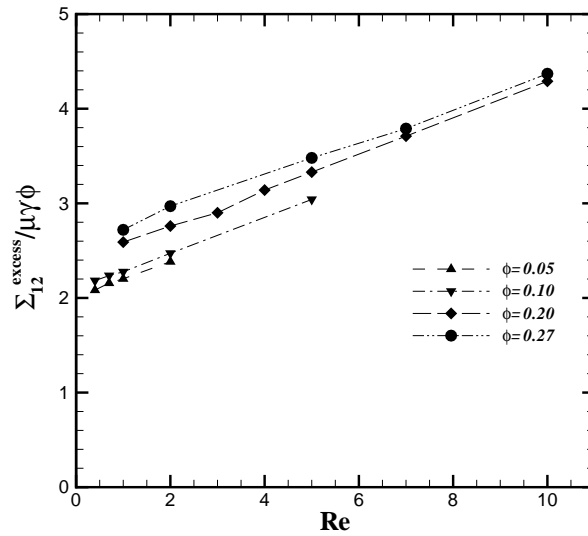


Figure 5.34: Σ_{xy}^{excess} variation with Re (Ca0.05 fixed)

Newtonian liquid, if the hydrodynamics conditions are close to Stokes flow, a positive resulting N_1 is responsible for a compressive forces on the bottom plate. Now, the

previous figure 5.32 indicates that even a small inertia (at the particle level) in the range of 2-5 is sufficient to develop a negative N_1 . Therefore in this case, one should expect a tensile force on the bottom plate.

Figure 5.35 shows the dependence of the excess stresses with volume fraction and the empirical relations are also presented by the use of curve fitting. Figure 5.36 shows the comparison of the viscosity ν /s volume fraction relation predicted by the simulation with the empirical relations provided by Pal [48]. He derived three empirical models and tested them against a range of experiments [49–56]. The third model in that paper was shown to give the best match with experiments. The current comparisons have also been made with the third model. Figure 5.36 shows that the comparison is quite good and the differences are in the range of 5%.

$$N_1 = 3.87\phi^2 - 0.172\phi - 0.03 \quad (5.5)$$

$$N_2 = -1.59\phi^2 + 0.082\phi \quad (5.6)$$

$$(5.7)$$

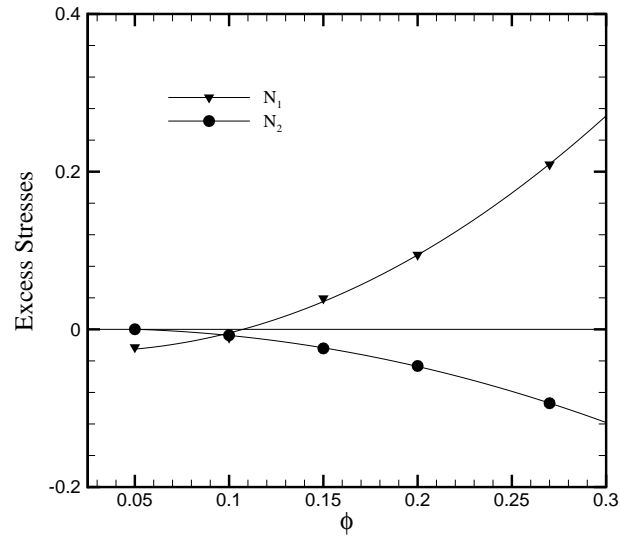


Figure 5.35: Dependence of the stresses on volume fraction (Re=1.0 and Ca=0.05)

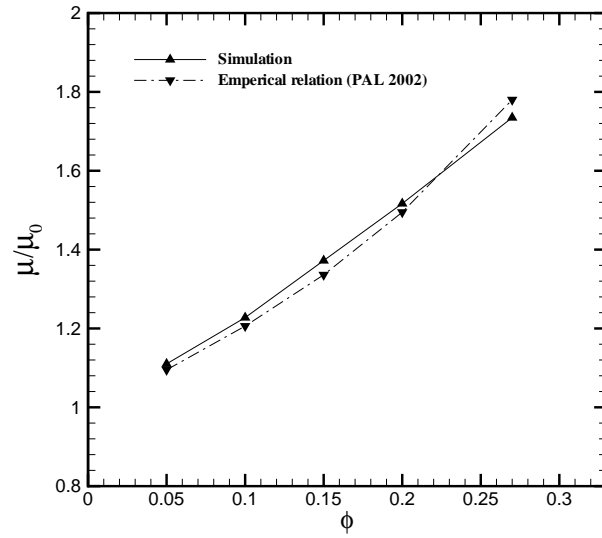


Figure 5.36: Dependence of the viscosity on volume fraction (Re=1.0 and Ca=0.05)

5.11 Relaxation Times

Emulsions exhibit non-Newtonian behaviour such as the presence of normal stress differences, shear rate dependent shear viscosity. Due to the interfacial tension, they also have associated with them a stress relaxation time. This means that if an emulsion is sheared and then the shearing is stopped after sometime, the stresses take a finite amount of time to die out even under Stokes flow condition. This is because it takes finite amount of time for the interfacial tension to restore the spherical shape of the droplets. Consequently this is a capillary time scale. Oldroyd [5] derived the expressions for the relaxation time using perturbation analysis. Choi and Schowalter [8] extended the results for relaxation time for a concentrated system. Almusallam et al. [11] performed relaxation experiments and calculated the stress relaxation time. Using this they fixed the unknown parameters in their phenomenological relations.

The current aim is to determine the relaxation times for a concentrated emulsion. To do this we first revisit the dilute emulsion problem containing a single drop and determine the stress relaxation time for this problem. After verifying these predictions, the relaxation time for a concentrated system is calculated. To determine the relaxation time the system is sheared to a steady state and then the shearing is stopped (numerically). Plotting the variation of the logarithm of the interfacial shear stress gives us the time scales for stress relaxation. Table 5.10 shows the variation of the time scale with different capillary numbers. The time scale predicted by Oldroyd i.e. $\tau_0 = \frac{(3+2\lambda)(16+19\lambda)a\mu}{40(\lambda+1)\Gamma} (\lambda = 1)$ is also shown in the table.

Table 5.9: Table showing relaxation time for a single drop problem, Re=0.05 fixed

capillary number	τ relaxation time	τ_0 (Oldroyd)	τ / τ_0
0.05	0.152	0.1094	1.390
0.10	0.240	0.2179	1.097
0.20	0.4796	0.4375	1.096

This table shows that the time scales obtained from the simulations agree well

with those predicted by Oldroyd. The value at $Ca=0.05$ is a bit higher. At this low capillary number the capillary time scale is very small. The ambient fluid too has associated with it a time scale for the decay of velocity field (viscous time scale) since we are not solving Stokes flow. So if the time scale for decay of the velocity gradient of the ambient fluid becomes close to the capillary time scale of the drops, then shear stresses may not relax according to the capillary time scale. This is what is happening for $Ca=0.05$.

After verifying the ability of the code to correctly predict the relaxation time for a dilute emulsion, a similar exercise is repeated for a concentrated emulsion at a volume fraction of 20%.

Table 5.10: Table showing relaxation time for $\phi = 20\%$, $Re=0.10$ fixed

capillary number	τ_0 (Oldroyd)	τ relaxation time	τ / τ_0
0.15	0.3281	0.5753	1.7535
0.20	0.4375	0.7475	1.708
0.25	0.5469	0.9043	1.6536

For the case of concentrated emulsion it should be noted that the relaxation time for the shear stress is higher than the Oldroyd's prediction. They are however closer to the value predicted by Choi-Schowalter model for a concentrated system ($\frac{\tau}{\tau_0} = 1.88$).

Chapter 6

ALTERNATE DIRECTION IMPLICIT METHOD

It was mentioned briefly in the chapter on front tracking method that the simulation time step is restricted by the viscous time limit criteria ($\delta t < \frac{0.125\rho\delta x^2}{\mu}$). This can be relieved by treating some of the viscous terms implicitly. This idea was followed in the serial version of the front tracking code [57]. A parallel version for this is presented here. This method involves the solution of tridiagonal matrices (including cyclic tridiagonal matrices associated with periodic boundary conditions). A simple algorithm (Thomas algorithm) for solving tridiagonal matrices is inherently serial in nature but even using this algorithm, the additional computational cost is outweighed by the benefits from the relaxed time stepping criteria. The following sections discuss the formulation of the Alternate Direction Implicit method (ADI) and then gives the procedure used for the numerical implementation.

6.1 Formulation

The first step for the projection method involves the following computation:

$$\frac{\rho^{n+1}\mathbf{u}^* - (\rho\mathbf{u})^n}{\delta t} = -\nabla \cdot (\rho\mathbf{u}\mathbf{u})^n + \nabla \cdot \tau^n + \mathbf{f}^n$$

Instead of treating all the viscous terms explicitly, only the cross terms are treated so. The remaining terms are considered implicitly. This is shown below:

$$\nabla \cdot \tau = \{D_{xx} + D_{yy} + D_{zz} + D_{xy} + D_{xz} + D_{yz}\}\mathbf{u}$$

Here $D_{xy} + D_{xz} + D_{yz}$ are the mixed terms and are treated explicitly. $D_{xx} + D_{yy} + D_{zz}$ are considered implicitly. So the first step of the projection method is itself subdivided

into a number of step where some of the viscous terms are treated implicitly one by one:

$$\frac{\rho^{n+1}\mathbf{u}^{****} - (\rho\mathbf{u})^n}{\delta t} = -\nabla \cdot (\rho\mathbf{u}\mathbf{u})^n + \{D_{xy} + D_{xz} + D_{yz}\}(\mathbf{u})^n + \mathbf{f}^n \quad (6.1)$$

$$\frac{\rho^{n+1}(\mathbf{u}^{***} - \mathbf{u}^{****})}{\delta t} = D_{xx}(\mathbf{u})^{***} \quad (6.2)$$

$$\frac{\rho^{n+1}(\mathbf{u}^{**} - \mathbf{u}^{***})}{\delta t} = D_{yy}(\mathbf{u})^{**} \quad (6.3)$$

$$\frac{\rho^{n+1}(\mathbf{u}^* - \mathbf{u}^{**})}{\delta t} = D_{zz}(\mathbf{u})^* \quad (6.4)$$

The following boundary condition is imposed for the intermediate velocity fields:

$$\mathbf{u}^* = \mathbf{u}^{**} = \mathbf{u}^{***} = \mathbf{u}^{****} = \mathbf{u}^{n+1} \quad (6.5)$$

Equations 6.2 and 6.4 involve solving cyclic Tridiagonal matrices (due to periodic boundary conditions) and equation 6.3 involves the usual tridiagonal matrix (due to wall boundary condition). The solution procedure is outlined in the next section.

6.2 Procedure

Equation 6.3 which involves a simple tridiagonal system can be solved by the well known Thomas Algorithm. Equations 6.2 and 6.4 which involve cyclic tridiagonal matrices can be solved by the use of Sherman Morrison formula [58]. These are frequently used standard algorithms for the serial computation. A solution to equations 6.2, 6.3 and 6.4 using a parallel algorithm has other sophisticated approaches. Johnsson et al. [59] investigated the performances of different parallel implementations of the method. Van der Wijngaart [60] used the standard Thomas algorithm for the

solution of tridiagonal matrices in a parallel environment but they considered different decomposition strategies.

The domain decomposition of the current code is dictated by its main Navier Stokes solver and the approach taken for the ADI was based on this decomposition. Therefore a simple parallel version of the Thomas algorithm (and the Sherman Morrison variant for periodic boundary conditions) was implemented. Though this involved a number of message passing steps, the use of derived datatypes helped in reducing the number of messages passed to some extent. The validations, computational efficiency and the time stepping benefits are presented below.

6.3 Validation

To validate the code with the ADI subroutines included, a simple single drop problem was studied. The domain size was fixed at roughly $10a$, grid resolution at $128 \times 128 \times 128$. The capillary number was kept at 0.05. The density (density ratio is unity) was varied to decrease the kinematic viscosity as the viscous time step criteria depends inversely on this parameter. Two cases were considered. The first case (figure 6.1) was for a density value which gave viscous time step criteria of $1E-03$. The plots below show the results for the interfacial stresses (Reynolds stresses were also checked but are avoided here) with and without ADI. The curves overlap which show that the method has been correctly implemented.

A second case (figure 6.2) was considered which gave a time step criteria of $0.38E-04$ and the plots show that the curves are very close. Slight differences are there because the simulation without ADI is run at the time step of $0.38E-04$ while the simulation incorporating the ADI method was still simulated at $1E-03$ (no stability issue) time step. This shows that the method is still stable. Infact the method is stable for a case in which time stepping criteria was as restrictive as $0.38E-05$. Therefore it can be concluded that the inclusion of the ADI subroutines gives at least an order of magnitude time stepping benefit.

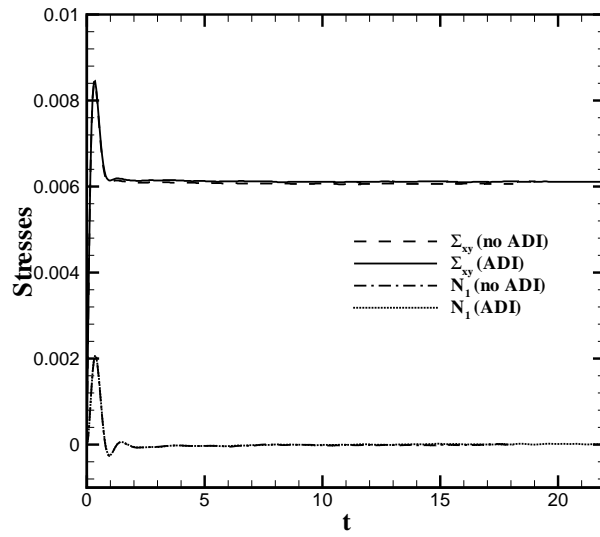


Figure 6.1: Validation of the ADI scheme with the first case

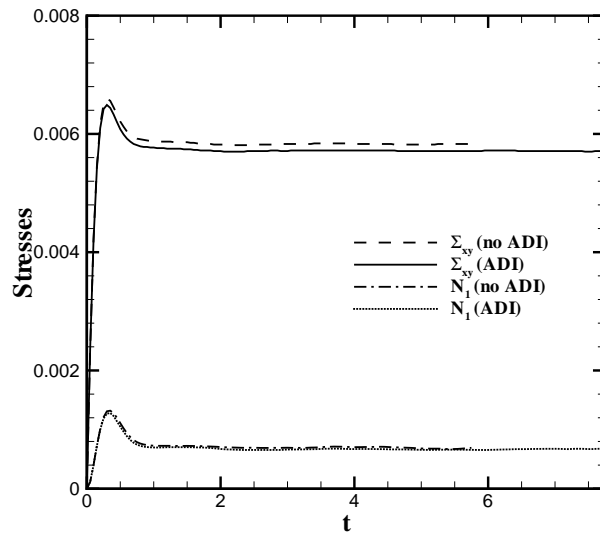


Figure 6.2: Validation of the ADI scheme with the second case

6.4 Computational Costs

The table below compares the computational cost of the ADI subroutines for unit cycle of computation. It presents the percentage of the total cost used by the ADI subroutines.

Table 6.1: Table showing the computational cost of the ADI method

No. of Procs	total time (s)	ADI time (s)	percentage
1	5.03	2.48	49
8	1.8	0.50	27
64	0.517	0.07	13

6.5 Conclusion

The main conclusion that can be drawn from the above data is that the fraction of the additional computational cost of the ADI method can be reduced if more processors are used. In such case the time stepping benefit completely outweighs the extra computational costs.

Chapter 7

SUMMARY AND FUTURE WORK

7.1 Summary

A computational study of the rheology of concentrated emulsions was undertaken with the use of a finite difference based front tracking method. A simple emulsion system consisting of Newtonian drops dispersed in a Newtonian matrix liquid is considered and even such a simple system exhibits complex non Newtonian behaviour. The constitutive relations for the emulsion was studied under a shearing condition. The effective properties were determined using Batchelor stress formulation.

The bulk stress was estimated for a range of volume fractions, capillary numbers and Reynolds number. The behaviour of the individual stress components (of the stress formulation): interfacial stresses and Reynolds stresses was studied under different conditions. The interfacial stresses exhibit interesting behaviours under increasing inertial effects. The interfacial first normal stress difference decreased and became negative with increasing Reynolds number. The interfacial second normal stress difference exhibited an opposite trend. Increasing concentration resulted in a larger first normal stress difference and consequently increasing volume fraction delayed the reversal of the signs of the normal stress differences. Interfacial shear stress exhibited a shear thickening behaviour with increasing Reynolds number and it also increased with volume fraction. Since the interfacial stresses are geometric quantities, their behaviour was explained by looking at simple geometric parameters like the average deformation and average orientation. Increasing inertia resulted in drops aligned along the velocity gradient direction and this was responsible for the reversal of the signs of the normal stress differences. Increasing inertia resulted in larger deformation which caused

a shear thickening behaviour. Increasing capillary number resulted in drops aligned towards the flow direction and consequently larger first normal stress difference and small shear stress (i.e. a shear thinning behaviour) was observed.

Reynolds stresses which form the second component of the stress formulation was also considered in detail. These stresses showed a simple scaling with Reynolds number for moderate values of Reynolds number. Beyond that range they showed a non-linear increase. Increasing capillary number increased the disturbances along the x direction and caused the Reynolds stress involving the x-component velocity to increase. It was also observed that the Reynolds stresses showed a time scale for achieving a steady value and this decreased with increasing inertia. The excess stress which is the total contribution to the bulk stresses from the drops presence is composed of both the interfacial and Reynolds stresses. It was noted that for low values of Reynolds number, the excess stress behaviour was dictated by interfacial stresses and beyond a Re of 2–5 the behaviour was completely governed by Reynolds stresses. This range of Re also depended on the volume fraction. The comparisons of the effective viscosity with some established empirical relations was also quite good. Stress relaxation time was also studied and comparisons were made against the standard relaxation time theoretical expressions.

Finally to improve the capabilities of the existing code to deal with extremely low Reynolds number flows a parallel version of the Alternate Direction Implicit method was implemented and tested .

7.2 Future Work

In this study a range of different parameters was considered to investigate the emulsion rheology. However there is scope for a number of different studies without major modification in the tools (code as well as theory) used in the current study.

7.2.1 Shear-induced self-diffusion

Brownian forces lead to diffusion of particles. For emulsions, the size of drops are large enough for the Brownian effects to be insignificant. Shearing forces result in a different type of diffusion termed as self diffusion which markedly affects the mixing properties of emulsions [61]. Therefore a rigorous investigation of this property has significant practical applications. Accurate prediction of the shear induced diffusion involves the use of very large number of drops [39] which the current study lacks. However the parallel code should be able to tackle this easily.

7.2.2 Rheology in poiseulle flow

The focus of the current research was to understand the behaviour and the dynamics of emulsions under shearing conditions. A systematic study can also be made for Poiseuille flow. The principle difference between these two is the existence of non-uniform shearing condition in Poiseuille flow. This results in interesting phenomena like shear-induced migration, which has been investigated in detail for rigid particle suspensions [62]. The current code is well suited for this type of problem since the existence of wall boundary conditions will no longer be an issue.

References

- [1] C. L. Tucker III and P. Moldenaers. Microstructural evolution in polymer blends. *Annual Review of Fluid Mechanics*, 34(1):177–210, 2002.
- [2] M. Loewenberg and E. J. Hinch. Numerical simulation of a concentrated emulsion in shear flow. *Journal of Fluid Mechanics*, 321:395–419, 1996.
- [3] G. I. Taylor. The Viscosity of a Fluid Containing Small Drops of Another Fluid. *Proceedings of the Royal Society of London. Series A, Containing Papers of a Mathematical and Physical Character*, 138(834):41–48, 1932.
- [4] A. Einstein. Eine neue bestimmung der moleküldimensionen. *Annalen der Physik*, 324(2):289–306, 1906.
- [5] J. G. Oldroyd. The Elastic and Viscous Properties of Emulsions and Suspensions. *Proceedings of the Royal Society of London. Series A, Mathematical and Physical Sciences*, 218(1132):122–132, 1953.
- [6] W. R. Schowalter, C. E. Chaffey, and H. Brenner. Rheological behavior of a dilute emulsion. *Journal of Colloid and Interface Science*, 26(2):152–160, 1968.
- [7] N. A. Frankel and A. Acrivos. The constitutive equation for a dilute emulsion. *Journal of Fluid Mechanics*, 44(01):65–78, 1970.
- [8] S. J. Choi and W. R. Schowalter. Rheological properties of nondilute suspensions of deformable particles. *Physics of Fluids*, 18(4):420–427, 1975.
- [9] M. Doi and T. Ohta. Dynamics and rheology of complex interfaces. I. *The Journal of Chemical Physics*, 95(2):1242–1248, 1991.
- [10] P. L. Maffettone and M. Minale. Equation of change for ellipsoidal drops in viscous flow. *Journal of Non-Newtonian Fluid Mechanics*, 78(23):227–241, 1998.
- [11] A. S. Almusallam, R. G. Larson, and M. J. Solomon. A constitutive model for the prediction of ellipsoidal droplet shapes and stresses in immiscible blends. *Journal of Rheology*, 44(5):1055–1083, 2000.
- [12] M. Iza and M. Bousmina. Nonlinear rheology of immiscible polymer blends: step strain experiments. *Journal of Rheology*, 44:1363, 2000.

- [13] J. F. Brady and G. Bossis. Stokesian dynamics. *Annual Review of Fluid Mechanics*, 20:111–157, 1988.
- [14] T. N. Phung, J. F. Brady, and G. Bossis. Stokesian Dynamics simulation of Brownian suspensions. *Journal of Fluid Mechanics*, 313:181–207, 3 1996. ISSN 1469-7645.
- [15] I. E. Zarraga, D. A. Hill, and D. T. Leighton Jr. The characterization of the total stress of concentrated suspensions of noncolloidal spheres in Newtonian fluids. *Journal of Rheology*, 44:185, 2000.
- [16] H. Zhou and C. Pozrikidis. The flow of ordered and random suspensions of two-dimensional drops in a channel. *Journal of Fluid Mechanics*, 255:103–127, 1993.
- [17] A. Z. Zinchenko and R. H. Davis. Shear flow of highly concentrated emulsions of deformable drops by numerical simulations. *Journal of Fluid Mechanics*, 455: 21–61, 2002.
- [18] C.-J. Lin, J. Peery, and W. Showalter. Simple shear flow round inertial effects and suspension rheology. *Journal of Fluid Mechanics*, 44(part 1):1–17, 1970.
- [19] N. A. Patankar and H. H. Hu. Finite Reynolds number effect on the rheology of a dilute suspension of neutrally buoyant circular particles in a Newtonian fluid. *International Journal of Multiphase Flow*, 28(3):409–425, 2002.
- [20] Y. Y. Renardy and V. Cristini. Effect of inertia on drop breakup under shear. *Physics of Fluids*, 13:7, 2001.
- [21] X. Li and K. Sarkar. Effects of inertia on the rheology of a dilute emulsion of drops in shear. *Journal of Rheology*, 49(6):1377–1394, 2005.
- [22] R. V. Raja, G. Subramanian, and D. L. Koch. Inertial effects on the rheology of a dilute emulsion. *Journal of Fluid Mechanics*, 646:255, 2010.
- [23] R. K. Singh and K. Sarkar. Inertial effects on the dynamics, streamline topology and interfacial stresses due to a drop in shear. *Journal of Fluid Mechanics*, 683: 149–171, 2011.
- [24] W. J. Rider and D. B. Kothe. Reconstructing volume tracking. *Journal of Computational Physics*, 141(2):112–152, 1998.
- [25] J. A. Sethian. *Level set methods and fast marching methods: evolving interfaces in computational geometry, fluid mechanics, computer vision, and materials science*, volume 3. Cambridge university press, 1999.
- [26] M. Sussman and E. G. Puckett. A coupled level set and volume-of-fluid method for computing 3D and axisymmetric incompressible two-phase flows. *Journal of Computational Physics*, 162(2):301–337, 2000.

- [27] G. Tryggvason, B. Bunner, A. Esmaeeli, D. Juric, N. Al-Rawahi, W. Tauber, J. Han, S. Nas, and Y.-J. Jan. A Front-Tracking Method for the Computations of Multiphase Flow. *Journal of Computational Physics*, 169(2):708 – 759, 2001. ISSN 0021-9991.
- [28] X. Li and K. Sarkar. Negative normal stress elasticity of emulsions of viscous drops at finite inertia. *Physical Review Letters*, 95(25):256001, 2005.
- [29] X. Li and K. Sarkar. Drop dynamics in an oscillating extensional flow at finite Reynolds numbers. *Physics of Fluids*, 17:027103, 2005.
- [30] X. Li and K. Sarkar. Numerical investigation of the rheology of a dilute emulsion of drops in an oscillating extensional flow. *Journal of Non-newtonian Fluid Mechanics*, 128(2):71–82, 2005.
- [31] X. Li and K. Sarkar. Drop deformation and breakup in a vortex at finite inertia. *Journal of Fluid Mechanics*, 564:1–24, 2006.
- [32] P. O. Olapade, R. K. Singh, and K. Sarkar. Pairwise interactions between deformable drops in free shear at finite inertia. *Physics of Fluids*, 21:063302, 2009.
- [33] R. K. Singh and K. Sarkar. Effects of viscosity ratio and three dimensional positioning on hydrodynamic interactions between two viscous drops in a shear flow at finite inertia. *Physics of Fluids*, 21:103303, 2009.
- [34] B. Bunner and G. Tryggvason. Direct numerical simulations of three-dimensional bubbly flows. *Physics of Fluids*, 11(8):1967–1969, 1999.
- [35] B. Bunner and G. Tryggvason. Dynamics of homogeneous bubbly flows part 1. rise velocity and microstructure of the bubbles. *Journal of Fluid Mechanics*, 466 (17-52):140, 2002.
- [36] B. Bunner and G. Tryggvason. Effect of bubble deformation on the properties of bubbly flows. *Journal of Fluid Mechanics*, 495:77–118, 2003.
- [37] A. Esmaeeli and G. Tryggvason. A direct numerical simulation study of the buoyant rise of bubbles at O (100) Reynolds number. *Physics of Fluids*, 17:093303, 2005.
- [38] S. Chen and G. D. Doolen. Lattice Boltzmann method for fluid flows. *Annual Review of Fluid Mechanics*, 30(1):329–364, 1998.
- [39] J. R. Clausen, D. A. Reasor, and C. K. Aidun. The rheology and microstructure of concentrated non-colloidal suspensions of deformable capsules. *Journal of Fluid Mechanics*, 685:202–234, 2011.
- [40] G. K. Batchelor. The stress system in a suspension of force-free particles. *Journal of Fluid Mechanics*, 41(03):545–570, 1970.

- [41] C. S. Peskin. Numerical analysis of blood flow in the heart. *Journal of Computational Physics*, 25(3):220–252, 1977.
- [42] G. Tryggvason, B. Bunner, O. Ebrat, and W. Tauber. Computations of multiphase flows by a finite difference/front tracking method. I. Multi-fluid flows. *Lecture Series-von Karman Institute For Fluid Dynamics*, pages 7–7, 1998.
- [43] P. C. H. Chan and L. G. Leal. An experimental study of drop migration in shear flow between concentric cylinders. *International Journal of Multiphase Flow*, 7(1):83–99, 1981.
- [44] J. R. Smart and J. D. T. Leighton. Measurement of the drift of a droplet due to the presence of a plane. *Physics of Fluids A: Fluid Dynamics*, 3(1):21–28, 1991.
- [45] V. Sibillo, G. Pasquariello, M. Simeone, V. Cristini, and S. Guido. Drop Deformation in Microconfined Shear Flow. *Physical Review Letters*, 97(5):054502, 2006.
- [46] P. Janssen and P. Anderson. Boundary-integral method for drop deformation between parallel plates. *Physics of Fluids*, 19:043602, 2007.
- [47] C. D. Han and R. G. King. Measurement of the Rheological Properties of Concentrated Emulsions. *Journal of Rheology*, 24(2):213–237, 1980.
- [48] R. Pal. Viscous behavior of concentrated emulsions of two immiscible Newtonian fluids with interfacial tension. *Journal of Colloid and Interface Science*, 263(1):296–305, 2003.
- [49] R. Pal. Rheological behaviour of concentrated surfactant solutions and emulsions. *Colloids and Surfaces*, 64(34):207 – 215, 1992. ISSN 0166-6622.
- [50] R. Pal. Rheological Properties of Emulsions of Oil in Aqueous Non-Newtonian Polymeric Media. *Chemical Engineering Communications*, 111(1):45–60, 1992.
- [51] R. Pal. Viscoelastic properties of polymer-thickened oil-in-water emulsions. *Chemical Engineering Science*, 51(12):3299 – 3305, 1996. ISSN 0009-2509.
- [52] P. Vergne, M. Kamel, and M. Querry. Behavior of cold-rolling oil-in-water emulsions: A rheological approach. *Journal of Tribology*, 119(2):250–258, 1997.
- [53] H. Eilers. The viscosity of emulsions made of highly viscous materials as a function of concentration. *Kolloid*, 97:313–321, 1941.
- [54] A. Leviton and A. Leighton. Viscosity relationships in emulsions containing milk fat. *Journal of Physical Chemistry*, 40(1):71–80, 1936.
- [55] R. Pal. Multiple O/W/O emulsion rheology. *Langmuir*, 12(9):2220–2221, 1996.

- [56] R. Pal. Shear Viscosity Behavior of Emulsions of Two Immiscible Liquids. *Journal of Colloid and Interface Science*, 225(2):359 – 366, 2000. ISSN 0021-9797.
- [57] K. Sarkar and W. R. Schowalter. Deformation of a two-dimensional drop at non-zero Reynolds number in time-periodic extensional flows: numerical simulation. *Journal of Fluid Mechanics*, 436(1):177–206, 2001.
- [58] W. H. Press, S. A. Teukolsky, W. T. Vetterling, and B. P. Flannery. *Numerical recipes 3rd edition: The art of scientific computing*. Cambridge University Press, 2007.
- [59] S. L. Johnsson, Y. Saad, and M. H. Schultz. Alternating direction methods on multiprocessors. *Siam Journal on Scientific and Statistical Computing*, 8(5):686–700, 1987.
- [60] R. F. Van der Wijngaart. Efficient implementation of a 3-dimensional ADI method on the iPSC/860. In *Supercomputing'93. Proceedings*, pages 102–111. IEEE, 1993.
- [61] M. Loewenberg and E. Hinch. Collision of two deformable drops in shear flow. *Journal of Fluid Mechanics*, 338:299–315, 1997.
- [62] P. R. Nott and J. F. Brady. Pressure-driven flow of suspensions: simulation and theory. *Journal of Fluid Mechanics*, 275(1):157–199, 1994.

Appendix A

REPRINT PERMISSION LETTERS

A.1 Reprint Permission of Figure 1.3 (Chapter 1)

This is a License Agreement between priyesh srivastava ("You") and The Society of Rheology ("SoR") provided by Copyright Clearance Center ("CCC"). The license consists of your order details, the terms and conditions provided by The Society of Rheology , and the payment terms and conditions.

All payments must be made in full to CCC. For payment instructions, please see information listed at the bottom of this form.

License Number	3160900101323
Order Date	Jun 02, 2013
Publisher	American Institute of Physics
Publication	Journal of Rheology
Article Title	Nonlinear rheology of immiscible polymer blends: Step strain experiments
Author	M. Iza, M. Bousmina
Online Publication Date	Nov 1, 2000
Volume number	44
Issue number	6
Type of Use	Thesis/Dissertation
Requestor type	Student
Format	Electronic
Portion	Photograph/Image
Title of your thesis / dissertation	Shear Rheology of Concentrated Emulsions at Finite Inertia: A Numerical study
Expected completion date	Aug 2013
Estimated size (number of pages)	100
Total	0.00 USD